Monthly Notices
of the
ROYAL ASTRONOMICAL SOCIETY

MNRAS **428,** 1880–1910 (2013) doi:10.1093/mnras/sts125

The Herschel Virgo Cluster Survey – XII. FIR properties of optically selected Virgo cluster galaxies

R. Auld,[1⋆] S. Bianchi,[2] M. W. L. Smith,[1] J. I. Davies,[1] G. J. Bendo,[3] S. di Serego Alighieri,[2] L. Cortese,[4] M. Baes,[5] D. J. Bomans,[6] M. Boquien,[7] A. Boselli,[7] L. Ciesla,[7] M. Clemens,[8] E. Corbelli,[2] I. De Looze,[5] J. Fritz,[5] G. Gavazzi,[9] C. Pappalardo,[2] M. Grossi,[10] L. K. Hunt,[2] S. Madden,[11] L. Magrini,[2] M. Pohlen,[1,12] J. Verstappen,[5] C. Vlahakis,[13,14] E. M. Xilouris[15] and S. Zibetti[2]

[1]*School of Physics and Astronomy, Cardiff University, The Parade, Cardiff CF24 3AA*
[2]*INAF-Osservatorio Astrofisico di Arcetri, Largo Enrico Fermi 5, I-50125 Firenze, Italy*
[3]*UK ALMA Regional Centre Node, Jodrell Bank Centre for Astrophysics, School of Physics and Astronomy, University of Manchester, Oxford Road, Manchester M13 9PL*
[4]*European Southern Observatory, Karl-Schwarzschild Str. 2, D-85748 Garching bei Muenchen, Germany*
[5]*Sterrenkundig Observatorium, Universiteit Gent, Krijgslaan 281 S9, B-9000 Gent, Belgium*
[6]*Astronomical Institute, Ruhr-University Bochum, Universitaetsstr. 150, D-44780 Bochum, Germany*
[7]*Laboratoire d'Astrophysique de Marseille-LAM, Université d'Aix-Marseille & CNRS, UMR7326, 38 rue F. Joliot-Curie, F-13388 Marseille Cedex 13, France*
[8]*INAF-Osservatorio Astronomico di Padova, Vicolo dell'Osservatorio 5, I-35122 Padova, Italy*
[9]*Universita' di Milano-Bicocca, piazza della Scienza 3, I-20100 Milano, Italy*
[10]*CAAUL, Observatório Astronómico de Lisboa, Universidade de Lisboa, Tapada da Ajuda, P-1349-018 Lisboa, Portugal*
[11]*Laboratoire AIM, CEA/DSM-CNRS-Université Paris Diderot, Irfu/Service, Paris, F-91190 Gif-sur-Yvette, France*
[12]*Gemini Observatory, Northern Operations Center, 670 N. A'ohoku Place, Hilo, HI 96720, USA*
[13]*Joint ALMA Observatory, Alonso de Cordova 3107, Vitacura, Santiago, Chile*
[14]*European Southern Observatory, Alonso de Cordova 3107, Vitacura, Casilla 19001, Santiago 19, Chile*
[15]*Institute of Astronomy and Astrophysics, National Observatory of Athens, I. Metaxaand Vas. Pavlou, P. Penteli, GR-15236 Athens, Greece*

Accepted 2012 October 1. Received 2012 September 19; in original form 2012 February 14

ABSTRACT

The Herschel Virgo Cluster Survey (HeViCS) is the deepest, confusion-limited survey of the Virgo Cluster at far-infrared (FIR) wavelengths. The entire survey at full depth covers ∼55 deg^2 in five bands (100–500 μm), encompassing the areas around the central dominant elliptical galaxies (M87, M86 and M49) and extends as far as the NW cloud, the W cloud and the Southern extension. The survey extends beyond this region with lower sensitivity so that the total area covered is 84 deg^2. In this paper we describe the data, the data acquisition techniques and present the detection rates of the optically selected Virgo Cluster Catalogue (VCC). We detect 254 (34 per cent) of 750 VCC galaxies found within the survey boundary in at least one band and 171 galaxies are detected in all five bands. For the remainder of the galaxies we have measured strict upper limits for their FIR emission. The population of detected galaxies contains early as well as late types although the latter dominate the detection statistics. We have modelled 168 galaxies, showing no evidence of a strong synchrotron component in their FIR spectra, using a single-temperature modified blackbody spectrum with a fixed emissivity index ($\beta = 2$). A study of the χ^2 distribution indicates that this model is not appropriate in all cases, and this is supported by the FIR colours which indicate a spread in $\beta = 1$–2. Statistical comparison of the dust mass and temperature distributions from 140 galaxies with $\chi^2_{\rm d.o.f.=3} < 7.8$ (95 per cent confidence level) shows that late types have typically colder, more massive dust reservoirs; the early-type dust masses have a mean of $\log[\langle M\rangle/{\rm M}_\odot] = 6.3 \pm 0.3$,

⋆E-mail: robbie.auld@astro.cf.ac.uk

while for late types $\log[\langle M\rangle/\mathrm{M}_\odot] = 7.1 \pm 0.1$. The late-type dust temperatures have a mean of $\langle T\rangle = 19.4 \pm 0.2$ K, while for the early types, $\langle T\rangle = 21.1 \pm 0.8$ K. Late-type galaxies in the cluster exhibit slightly lower dust masses than those in the field, but the cluster environment seems to have little effect on the bulk dust properties of early types. In future papers we will focus more on the scientific analysis of the catalogue (e.g. measuring FIR luminosity functions, dust mass functions and resolved gas and dust properties).

Key words: dust, extinction – galaxies: clusters: individual: Virgo – galaxies: ISM – galaxies: photometry – infrared: galaxies.

1 INTRODUCTION

Of the major galaxy overdensities in the nearby Universe (Virgo, Fornax, Abell 1367, Ursa Major and Coma) the Virgo cluster remains the most widely studied. Its proximity (17 Mpc; Gavazzi et al. 1999) allows us both to probe the cluster population down to faint levels and to resolve the larger galaxies with modest instruments.

In contrast to other, more relaxed clusters, Virgo exhibits a relatively high fraction of gas-bearing galaxies. As the galaxies surrounding Virgo fall into the cluster they are subject to many interactions. Interactions with the cluster gravitational potential (Merritt 1984; Boselli & Gavazzi 2006), the hot intracluster medium (ICM; Gunn & Gott 1972; Abadi, Moore & Bower 1999) and, in some cases, each other (Moore et al. 1996; Mihos 2004) are among the dominant processes affecting evolution in the cluster. They are believed to be responsible for transforming galaxies from gas-bearing, star-forming late types into the dormant early-type galaxies that dominate the cluster core, but the details of these processes are still poorly understood.

Evidence of these interactions can be seen in the disturbed morphologies of the galaxies themselves (e.g. NGC 4438; Vollmer et al. 2001; Oosterloo & van Gorkom 2005) or in the ICM, where streams such as those observed in the optical (Mihos et al. 2005) and 21 cm (Gavazzi et al. 2008) show that the space between galaxies is littered with stellar and gaseous material. The other major interstellar medium (ISM) constituent, dust, is also expected to carry the signatures of these interactions. Understanding what happens to the dust component in the cluster environment is another important aspect of environmental effects on galaxy evolution, but requires a large data set of galaxies in different environments.

Dust emission dominates the mid-infrared (MIR, 1–10 μm) to far-infrared (FIR, 10–500 μm) and submillimetre (submm, 500–1000 μm) portion of a galaxy's spectral energy distribution (SED). In the MIR, it is a complicated mixture of thermal emission from stars and warm ($T \sim 30$ K) dust, and line emission from molecular species. The FIR and submm regime, however, is dominated by thermal emission from interstellar dust grains. Studying galaxies at these wavelengths has been problematic since ground-based observations are compromised by high attenuation and bright spectral line emission from the Earth's atmosphere.

Space missions such as *IRAS*, *ISO* and most recently *Spitzer* have been vital for expanding our understanding of interstellar dust. *IRAS* and *Spitzer* were sensitive to the warm dust (>30 K) within dust-bearing galaxies (e.g. Devereux & Young 1990; Kennicutt et al. 2003), while *Infrared Space Observatory* (*ISO*) and the ground-based Submillimetre Common-User Bolometer Array allowed astronomers to probe the coldest dust within galaxies (e.g. Alton et al. 1998; Dunne & Eales 2001; Dunne & Eales 2002; Popescu et al. 2002; Tuffs et al. 2002). Unfortunately these pioneering instruments were limited in their resolution and sensitivity, and these early studies were confined to individually targeted galaxies.

The Herschel Virgo Cluster Survey (HeViCS; Davies et al. 2010) has observed 84 deg^2 of the Virgo cluster with the primary goal of studying cold-dust-bearing galaxies in the cluster environment. The 3.5-m primary mirror of the *Herschel Space Observatory*, combined with the ability to perform five-band photometry simultaneously over a wavelength range of 100–500 μm, affords the survey unprecedented sensitivity and resolution in the FIR regime. This has enabled us to conduct the most detailed studies to-date of cold (<30 K) dust in Virgo cluster galaxies.

In previous work, based on shallow data from the central $4^\circ \times 4^\circ$ region, we have already analysed the FIR luminosity function in the cluster core (Davies et al. 2010), studied truncated dust discs in cluster galaxies (Cortese et al. 2010), put upper limits on the dust lifetime in early-type galaxies (Clemens et al. 2010), probed the distribution of dust mass and temperature within cluster spirals (Smith et al. 2010), identified an excess at 500 μm for a sample of metal-poor, star-forming dwarfs (Grossi et al. 2010), studied non-thermal FIR emission from the dominant cluster elliptical galaxy, M87 (Baes et al. 2010), and detected dust in cluster dwarf elliptical (dE) galaxies (de Looze et al. 2010).

In more recent work, based on the full survey area but limited in depth, we have presented an analysis of the brightest galaxies at 500 μm (Bright Galaxy Sample, BGS; Davies et al. 2012). We have examined the metallicity dependence of the molecular gas conversion factor, X_{CO} (Magrini et al. 2011), and probed the effect of interactions on the distribution of dust and gas in a sample of late types (Corbelli et al. 2012; Pappalardo et al. 2012),

In this, the first paper to exploit the full data set, we present the FIR properties of a statistically complete, optically selected sample, the Virgo Cluster Catalogue (VCC; Binggeli, Sandage & Tammann 1985). We concentrate on the description of the data, the data reduction, the flux measurements themselves and the recovery rates of the VCC galaxies. This will pave the way for future papers which will focus on the science that can be extracted from the data (FIR/submm colour relations, luminosity functions, dust mass functions, radial/resolved FIR properties, etc.).

The VCC is the largest and most reliable catalogue of cluster members; it covers 140 deg^2 and contains almost 1300 probable cluster galaxies. Membership was based, for most part, on morphological criteria, with redshift information taking precedence as it became available. A comparison of the morphology method with redshift data proved it to be very reliable, with a success rate of over 98 per cent (Binggeli et al. 1985; Binggeli, Popescu & Tammann 1993).

While it is true that the cluster has been observed with more sophisticated instruments with superior imaging capabilities compared to the original Las Campanas plates (e.g. Côté et al. 2004; Kim et al. 2011), the power of the catalogue lies in the membership information itself. Applying their optical completeness limit of photographic magnitude, $m_{\mathrm{pg}} \leqq 18$, yields a population of ∼1000 galaxies, and has provided the astronomical community with a large,

statistically complete sample of Virgo cluster galaxies. It has been used for nearly 30 yr with only minor revision (e.g. Binggeli et al. 1993; Gavazzi et al. 1999) and will only be surpassed by the completion of the Next Generation Virgo Survey (Mei et al. 2010; Ferrarese 2011).

The data for our optical comparisons were taken from the GOLDMINE data base (Gavazzi et al. 2003) which includes measurements at multiple wavelengths for the entire, revised VCC. It is our intention to expand the data base with our FIR measurements. By augmenting these data with the HeViCS data we aim to provide the community with a definitive legacy product that will enable the detailed study of stars and dust in the cluster environment.

In Section 2 we describe the survey data acquisition, data reduction, the flux extraction method and the SED fitting. In Section 3 we present the detection rates and the flux measurements at 100, 160, 250, 350 and 500 μm. In this section we also provide the results of the SED modelling and show the derived dust mass and temperature distributions for a subset of galaxies which were well fitted by the single-temperature model. In Section 4 we summarize our findings. The tables of fluxes and dust mass/temperature are attached as appendices in Tables B1 and C1. The FIR SED fits are displayed in Appendix D.

2 OBSERVATIONS, DATA REDUCTION AND FLUX MEASUREMENT

2.1 Observations

The HeViCS survey region constitutes four overlapping $4^\circ \times 4^\circ$ tiles (Fig.1) including the majority of cloud A, centred on M87 and extending far enough to encompass the NW cloud, the W cloud and the S extension in the nomenclature of de Vaucouleurs (1961). Each tile has been observed by the *Herschel* Photodetecting Camera and Spectrometer (PACS) (Poglitsch et al. 2010) and Spectral and Photometric Imaging Receiver (SPIRE) (Griffin et al. 2010) instruments operating in fast-parallel mode, allowing PACS and SPIRE photometry to be performed simultaneously at a scan rate of 60 arcsec s^{-1}. The observing strategy consists of scanning each $4^\circ \times 4^\circ$ tile in two orthogonal directions. This cross-linking allows for the application of data processing techniques that can mitigate the effects of $1/f$ noise. This enables the potential recovery of structure (cirrus/intracluster dust) of up to the length of a tile (4°). This strategy is then repeated until each tile is nominally covered by eight scans, although in overlap regions this can reach as high as sixteen scans.

The PACS footprint is offset from the SPIRE footprint by 20 arcmin, leading to slight mismatch in the area of sky surveyed. To compensate for this effect, the proposed survey target regions are automatically expanded at the observing stage, to reach full coverage with both instruments in the target field. This gives rise to extra data, outside the target region. We retain the extra data and after combining the entire set of cross-linked scans, the total sky coverage is somewhat larger than previously claimed ($\sim$84 deg^2 compared to 64 deg^2), although the full-depth region is limited to the central 55 deg^2.

2.2 Data reduction

The SPIRE photometer (Griffin et al. 2010) data were processed up to Level 1 (i.e. calibrated bolometer timelines) with a custom made pipeline adapted from the official pipeline.[1] The purpose of the pipeline is to remove all instrumental artefacts such as glitches, finite bolometer time response, electronic filtering and thermal drift, as well as applying astrometry and flux calibration.

The main difference between our pipeline and the standard one is that we did not run the default *temperatureDriftCorrection* and the residual, median baseline subtraction. Instead, we use a custom method called the BRIght Galaxy ADaptive Element (BriGAdE; Smith et al., in preparation) to remove the temperature drift. No further baseline subtraction was necessary to bring the bolometer baselines to a common level.

BriGAdE uses the information from the thermistors in each array and directly fits the thermistor data to the entire bolometer timeline (including data where the spacecraft was slewing between scans). If both thermistors exhibited instantaneous 'jumps' (an artefact where there is a sudden offset in the timelines), these are either corrected or the comparison switched to the slightly less sensitive dark pixels of the individual array. This approach is hampered slightly by the presence of bright sources in the bolometer timelines. To suppress their influence, they are automatically removed from the fitting process along with samples affected by other artefacts ('jumps' and glitches). When a choice of thermistors is available (i.e. for the 250 and 500 μm arrays), the one providing the best fit is used to subtract a scaled version from the bolometer timelines. This method improves the baseline subtraction significantly, especially in cases where there are large or rapid temperature variations during the observations, which cause large stripes in the final maps (Fig. 2).

The individual scans from all 32 cross-linked observations are combined into a single mosaic using the inbuilt naïve mapper of HIPE. The full width at half-maximum (FWHM) measurements of the beams in the final maps are 18.2, 25.4 and 36.0 arcsec for 250, 350 and 500 μm, respectively. The beam areas used in the conversion from Jy $beam^{-1}$ to Jy were 423, 751 and 1587 $arcsec^2$, at 250, 350 and 500 μm, respectively. This is in accordance with the SPIRE photometry guidelines.[2] The final maps have pixel sizes of 6, 8 and 12 arcsec at 250, 350 and 500 μm, respectively. One of the by-products of the HIPE data processing is a map of the instrumental noise. For the SPIRE bands this gives corresponding instrument-associated noise levels of 4.9, 4.9 and 5.7 mJy $beam^{-1}$ in the areas uniformly covered by eight scans. This drops to 3.5, 3.4 and 4.0 mJy $beam^{-1}$, in the overlapping regions, uniformly covered by 16 scans. The values are consistent with a drop in the noise level proportional to $\sqrt{(t)}$, where t is the integration time, demonstrating that the contamination by $1/f$ noise is minimal.

Deriving the global noise is not a straightforward task due to the presence of background source crowding and Galactic cirrus emission, which are both position dependent. We selected a region in the fully sampled southernmost tile, which had the lowest cirrus contribution. Within this region we measured pixel–pixel fluctuations and applied iterative 3σ clipping to eliminate the contribution from bright sources. This gave noise values of 6.6, 7.3 and 8.0 mJy $beam^{-1}$ (250, 350, and 500 μm, respectively). By quadratically subtracting the instrumental noise, we derived confusion noise estimates of 4.4, 5.4 and 5.6 mJy $beam^{-1}$ (250, 350 and 500 μm, respectively). These crude estimates are slightly higher than Nguyen et al. (2010) on the Hermes fields (3.8, 4.6 and 5.2 mJy $beam^{-1}$,

[1] See Griffin et al. (2010) or Dowell et al. (2010) for a more detailed description of the official pipeline and a list of the individual modules.

[2] http://herschel.esac.esa.int/twiki/pub/Public/SpireCalibrationWeb/beam_release_note_v1-1.pdf

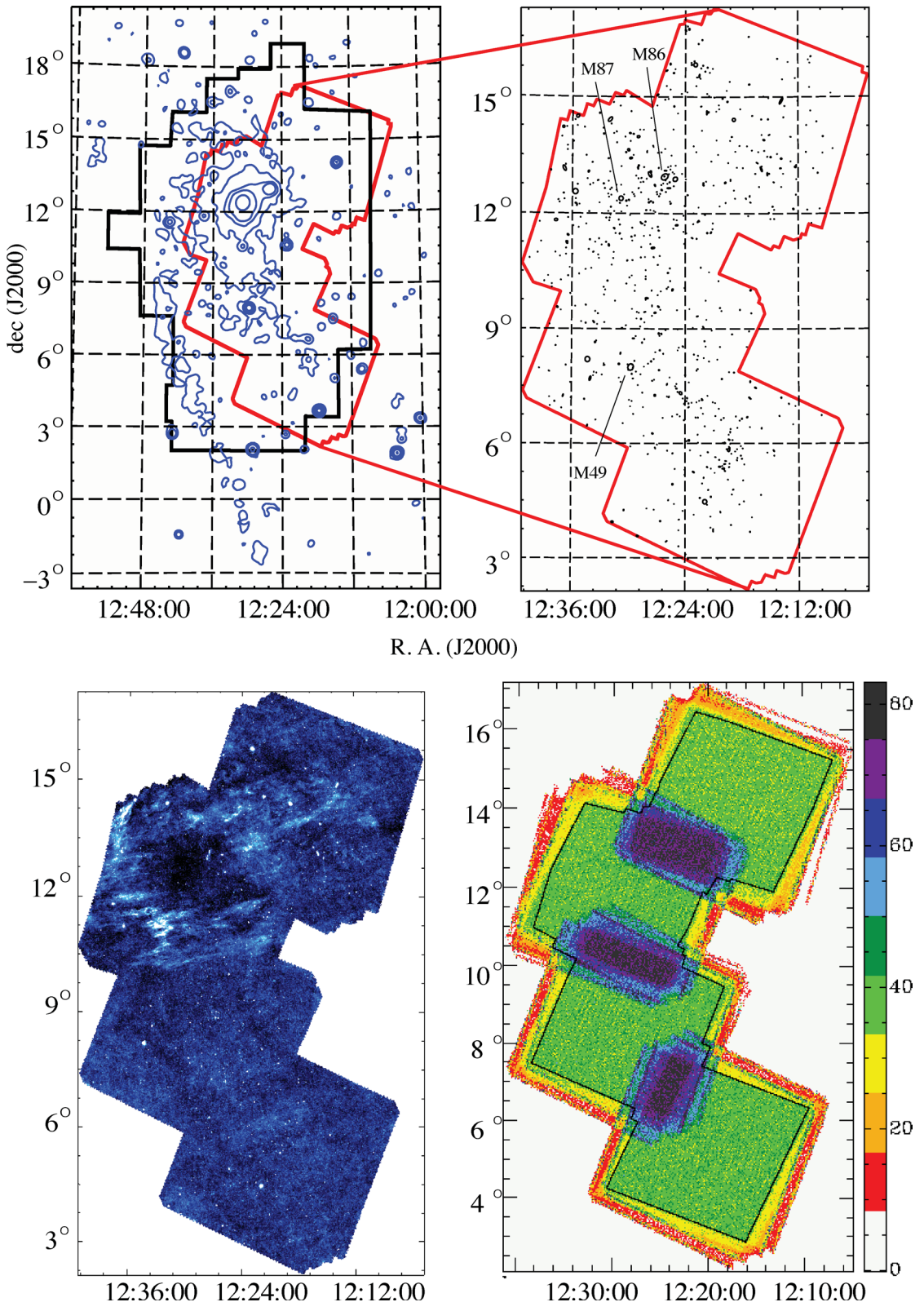

Figure 1. Top left: the Virgo cluster region. X-ray contours from Boehringer et al. are shown in blue. The VCC survey region is outlined in solid black and the full extent of HeViCS is outlined in red. Top right: the HeViCS survey region with black ellipses representing the VCC optical discs measured to d_{25}. The dominant cluster galaxies have been labelled and their positions correspond to the peaks in X-ray emission. Bottom left: *Herschel*-SPIRE 250 μm image of the full survey. Even in this small image it is possible to identify the VCC galaxies with the strongest FIR emission and the large swathes of Galactic dust cirrus. Bottom right: survey depth, measured in samples per pixel, from the 250 μm data. The inner region, covered by eight scans with PACS and SPIRE, is shown by the black outline. In the overlap region between tiles the coverage rises to 16 scans.

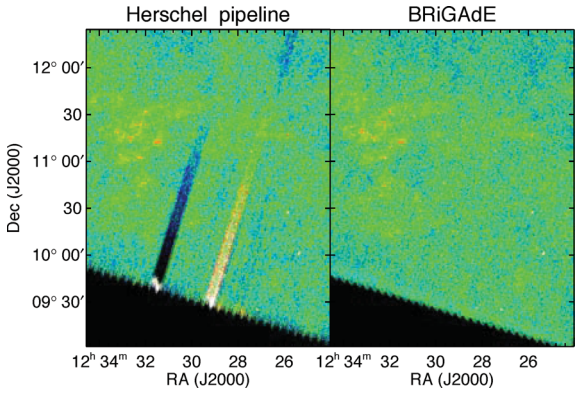

Figure 2. Instantaneous jumps in the thermistor timelines give rise to striping in the final images, when using the standard *Herschel* pipeline. Use of the BriGAdE method greatly reduces their impact.

respectively, employing an analogous iterative 3σ clip), but still within twice their quoted uncertainty. The HeVICS SPIRE maps have similar contributions from confusion and instrumental noise. We repeated the analysis on regions of overlap between the tiles, which have greater coverage and found no significant reduction in the noise level, implying that the maps are close to being dominated by confusion noise.

With regard to the PACS data, we have obtained maps at 100 and 160 μm by exploiting the naive projection task `photProject` in HIPE (v7.3.0), following a similar approach as described by Ibar et al. (2010). Map making was performed in two steps: for each single scan, we first obtained maps using the standard data reduction pipeline, but with the entire VCC galaxies masked out. In these maps, the $1/f$ noise was corrected for by applying a high-pass filter with a length of 20 and 40 frames for the 100 and 160 μm map, respectively, and deglitching was performed by means of the sigma-clipping standard algorithm (`IIndLevelDeglitchTask` task in HIPE, with $\sigma = 3$). These preliminary maps were used to identify and mask bright, extended non-VCC sources, and to fine-tune the deglitching. The masks were then applied to the calibrated timelines using a flux threshold set to 2.5σ, and the minimum number of pixels above the threshold, for a source to be detected, was set to 48 and 24 for the 100 and 160 μm channels, respectively. In order to minimize the high-pass filtering oversubtraction, the masks were enlarged, by adding 4 and 2 pixel to the edges of the detected sources, for 100 and 160 μm maps, respectively.

In a second step, the data were reduced again. This time, the deglitching task was applied before high-pass filtering, with the bright sources being masked to avoid unwanted flux removal from their brightest parts. Then, the masked, deglitched timelines were high-pass filtered, with a filter length of 10 and 20 frames for 100 and 160 μm, respectively. At this point the timelines for the eight scans were joined together. After this, the second-level deglitching task was run to remove glitches from the bright sources and, finally, individual tile maps were produced with the `photProject` task.

Due to the enormous volume of data in a PACS observation, the HIPE map maker is currently only capable of combining eight cross-scans from an individual tile into a single mosaic. The individual tiles were then combined into mosaics using the SWARP[3] package.

The PACS beams at 100 and 160 μm are elongated along the scan direction due to on-board averaging of the PACS data. This is a necessary complication due to the limit of the rate at which data can be downloaded from the spacecraft. Averaging together the eight-scan data, taken at different observing angles, results in approximately circular beams. These are Gaussian in shape with FWHM values for the 100 and 160 μm beams of 9.4 and 13.4 arcsec, respectively, and the corresponding map pixel sizes are 2 and 3 arcsec. The PACS instrumental error maps from the HIPE pipeline are still in the process of being optimized, so PACS errors were estimated directly from the signal maps, using apertures on blank regions of sky. The standard deviations of the background in the PACS maps are 1.9 and 1.2 mJy pixel^{-1} for the 160 and 100 μm channels, respectively, in the areas covered by eight scans. This decreases to 1.3 and 0.8 mJy pixel^{-1} in the overlapping regions. This is consistent with a $\sqrt{t_{\rm int}}$ decrease, where $t_{\rm int}$ is the integration time, indicating that the noise in the background in the PACS maps is still dominated by instrumental noise.

2.3 Flux measurement

Of the 1076 VCC objects with $m_{\rm pg} \leqq 18$, 750 fall within the extreme boundary of the HeViCS region. Once these targets were identified, the optical parameters (position, ellipticity, position angle and optical diameter – d_{25}) were used to overplot the optical disc on the 250 μm image. Position angles for the VCC galaxies were obtained from HyperLEDA. The d_{25} was taken from the original VCC as quoted in GOLDMINE, which has been estimated from the photographic plates. Previous studies (e.g. Cortese et al. 2010; Pohlen et al. 2010) have shown that the optical emission is fairly well traced by the FIR emission, for late-type galaxies without truncated gas discs. Preliminary comparisons between the optical and FIR emission for HeViCS late-type galaxies revealed that the optical ellipse parameters provided a good basis for defining the FIR apertures for measuring the flux. Early types tended to exhibit point-like emission in the FIR, and in a few particular cases irregular and extended (e.g. M86) or dominated by synchrotron radiation from the active galactic nucleus (AGN) jets (e.g. M87; Baes et al. 2010).

Accurate photometry had to be able to cope with several aspects inherent to the *Herschel* images. The SPIRE maps are dominated by Galactic cirrus and, to a lesser extent, by unresolved background sources. Some bright sources in the PACS images also suffer from negative bowls which are the result of inaccurate masking of bright sources during the high-pass filtering. Various stages of the measurement process are displayed in Fig.3. It may aid the reader to refer to this during the description that follows.

To begin with, a 200 × 200 pixel sub-image centred on each galaxy was extracted from the full map (Fig. 3a). The galaxy was then masked as are all the nearby Virgo galaxies. The extent of the galaxy was defined by the $1.5 \times d_{25}$ limit. It should be noted that there can be small differences between this d_{25} measurement (estimated from photographic plates) and the equivalent measured from CCD data. The difference is not important to us, however, since the ellipticity and extent are merely used as starting points for the ellipse measuring procedure. To account for edge-on galaxies and those whose optical dimensions were smaller than the beam at any given wavelength, the optical ellipse parameters were convolved with a Gaussian beam profile of the relevant size for each band. In some cases, the optical morphology was unrepresentative of the FIR emission (e.g. for point-like or irregular sources). For bright, point-like sources, circular ellipses were employed and for M86, we used the features identified in Gomez et al. (2010) to define the extent of emission in M86. For cases where the optical extent was too large to elicit a reliable estimate of the background, the

[3] http://www.astromatic.net/software/swarp

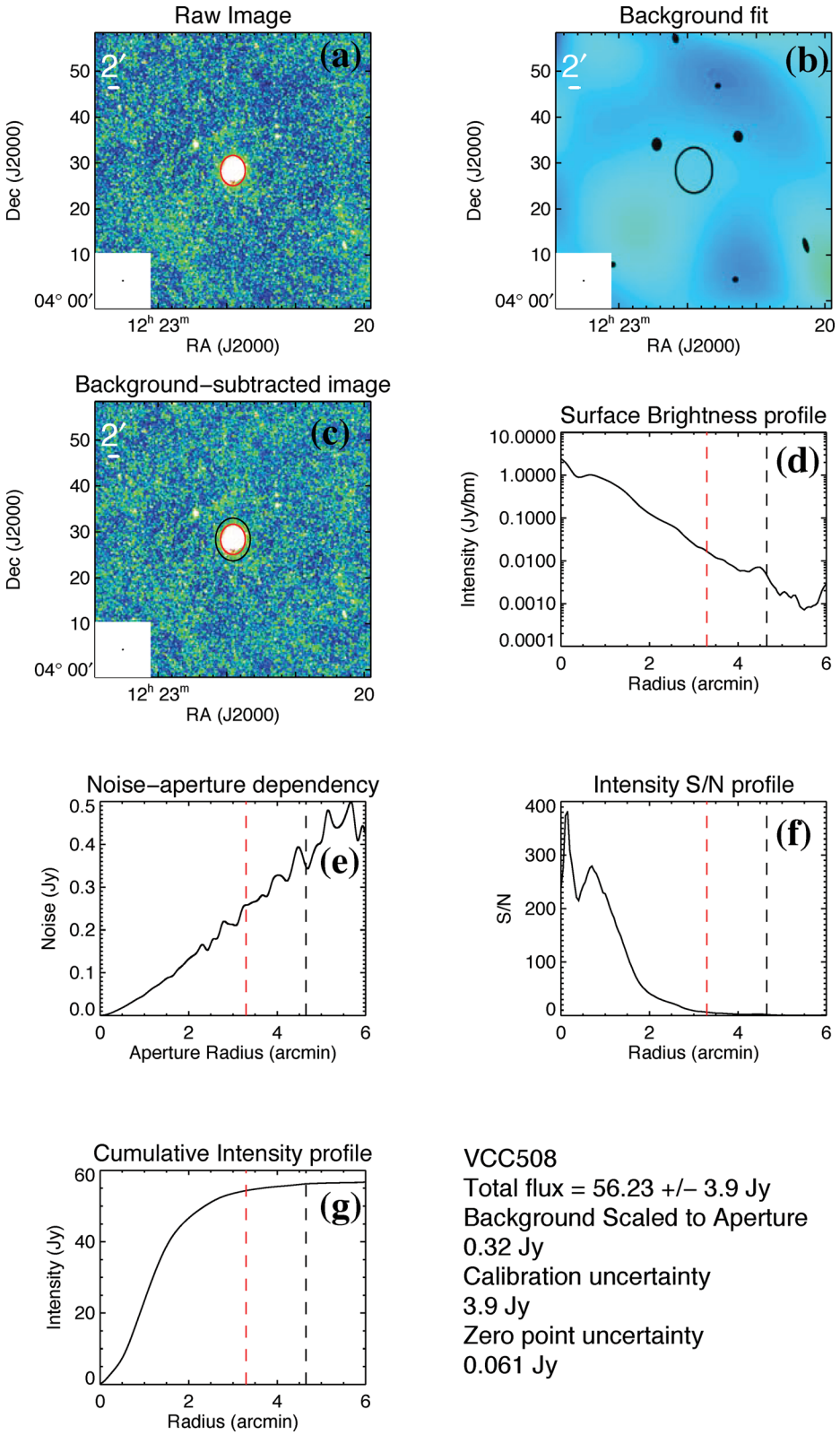

Figure 3. Example products from the fitting process for M61 (VCC 508) at 250 μm. (a) The raw sub-image extracted from the full HeViCS mosaic. The d_{25} limit is outlined in red, the 250 μm beam is given to scale at the bottom left of the image. (b) The estimate of the background from the masked image. The ellipse is explained in the text. (c) The resultant background-subtracted sub-image on which radial plots and flux measurements are performed. (d) Radial plot of surface brightness. (e) Radial dependence of the total noise in a circular aperture. (f) and (g) Radial plots of S/N and cumulative intensity, respectively. Optical (d_{25}) and FIR limits are indicated by the red and black dashed lines, respectively.

sub-image region was increased to 600 pixel for SPIRE and up to 1200 pixel for PACS maps.

The background is a combination of the foreground cirrus, bright background sources and unresolved background sources. For SPIRE images which are highly confused, the estimate of the background was achieved with a fifth-order (i.e. terms up to x^5, y^5 plus all cross terms) 2D polynomial over the entire masked sub-image. We employed the least-squares polynomial fitting IDL routine SFIT to perform the fit. To counteract the influence of bright background galaxies a 95 per cent flux clip was imposed and the remaining pixels used to estimate the background. For PACS images which were dominated by instrumental noise, a second-order polynomial was adequate. An example of the background estimate is shown in Fig. 3(b). Once the background estimation was obtained, it was subtracted from the original sub-image (Fig. 3 c).

We then created annuli based on the optical ellipse parameters at increasing radii around the optical centre of the galaxy. For each annulus we measured the total flux, the surface brightness, the aperture noise (described in Section 2.4.2) and the signal-to-noise ratio (S/N). The S/N was calculated as the ratio of the total flux within the annulus to the noise in an aperture with the same area as the annulus.

The S/N radial profile was then used to define a cut-off once the S/N dropped below 2. This is then used to define the edge of the galaxy (the black dashed line in Figs 3 d–g). The final measured uncertainty is then calculated from the quadrature sum of the aperture noise for the entire aperture, the calibration uncertainty and the zero-point error. The new estimate of the galaxy edge is used to create a new mask, replacing the old $1.5 \times d_{25}$ limit, and the process repeated. Once the procedure converged, aperture corrections were applied to the flux and the aperture noise measurements in accordance with Ibar et al. (2010) and Griffin & North (in preparation).

If the total aperture S/N measured less than 3, using this method, the sub-image was optimally searched again for a point source. This consisted of convolving each sub-image with the relevant point spread function (PSF) for each band and measuring the peak emission within an area defined by the convolved PSF FWHM, centred on the optical position. To measure the noise in the PSF-convolved map we plotted the histogram of the flux values and fit the negative flux values with a Gaussian function, whose width is representative of the combined instrumental and confusion noise (Marsden et al. 2009; Chapin et al. 2011, and references therein). In practice this required some tuning, the best results being achieved when fitting a Gaussian to a reduced range of histogram bins that encompassed a significant portion of the negative tail, the peak and a small number of bins on the positive side of the peak. The width of this Gaussian was then taken as our estimate of the noise, and detections were defined as those sources above 3σ. In the case of a detection, the noise from the PSF-convolved map was summed in quadrature with the calibration uncertainty and zero-point uncertainty to provide the total error. If the source was still undetected, the 3σ upper limit was measured from the histogram in the PSF-convolved map.

We recorded all of the radial data and intermediate masks during the process and, they will be publicly available online[4] in ASCII format as well as *eps* figures outlining the different steps, such as that shown in Fig. 3.

Once the automatic flux measurements were completed each detected galaxy was analysed by-eye to confirm that the masking and cut-off radius were realistic. Optical images from GOLDMINE and

[4] http://goldmine.mib.infn.it/

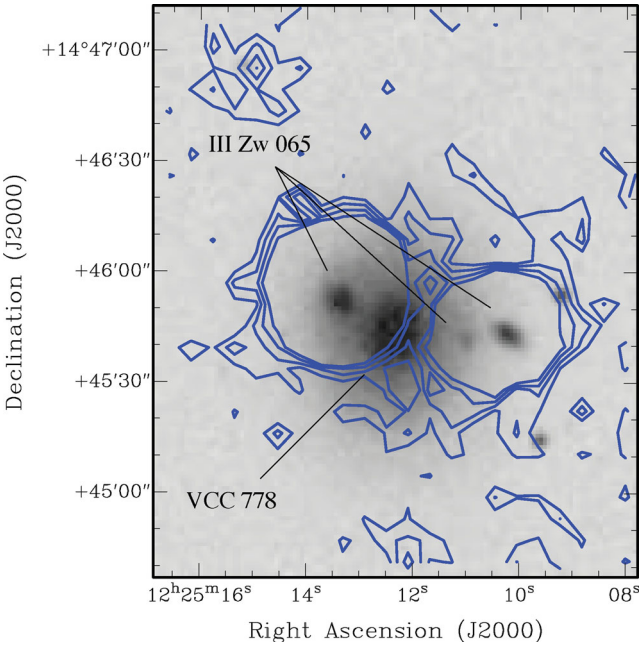

Figure 4. An example of background confusion causing an incorrect detection. A DSS grey-scale image overlaid with 250 μm contours at 0.005, 0.01, 0.015 and 0.02 Jy beam^{-1}. The target early-type galaxy, VCC 778, is sandwiched between a background triplet (listed in NED as III Zw 065). Their FIR emission dominates the total flux in this region; hence the emission from VCC 778 is not well determined.

the Digital Sky Survey were examined in order to make the most comprehensive judgment for discriminating between background sources and galactic features. We found that occasionally the algorithm could be deceived by nearby, bright background galaxies or by the presence of bright cirrus which was insufficiently modelled and removed. Some were obvious as in the case of VCC 778 (Fig. 4); here the FIR emission consists of multiple point sources with optical background galaxies clearly visible near the centre of the emission. Some were more ambiguous as in VCC 355 (Fig. 5); while this galaxy does have FIR emission within the optical extent of the galaxy, it is in a highly confused region and there is nothing to distinguish it from the immediate background. For these sorts of detections, human intervention was required to define the radial cut-off manually or to exclude the galaxy from the list of detections. This affected ∼10 per cent of the total number of measurements, most of which were false detections. In the event that the galaxy was excluded due to a contaminating source, the measured flux of the contaminating source at the position of the galaxy has been recorded as the upper limit and these sources are labelled with an asterisk in Table B1.

Since the 250 μm data have the best combination of sensitivity and resolution, we also imposed a strict requirement that a galaxy be detected at 250 μm. This further restricts the possibility of illegitimate background sources making it into the catalogue.

The FIR emission from the interacting galaxy pair NGC 4567/8 (VCC 1673/6) is a confused system with overlapping contributions from both galaxies. We have adapted the method described above to model NGC 4567 and hence measure the individual fluxes. This method is fully described in Appendix A.

The nominal SPIRE and PACS flux calibration schemes assume a 'white' point source, i.e. a compact object whose emission is flat across the filter bandpass (the K4 term). This term varies as a function of the object size and spectral index, and so must be corrected

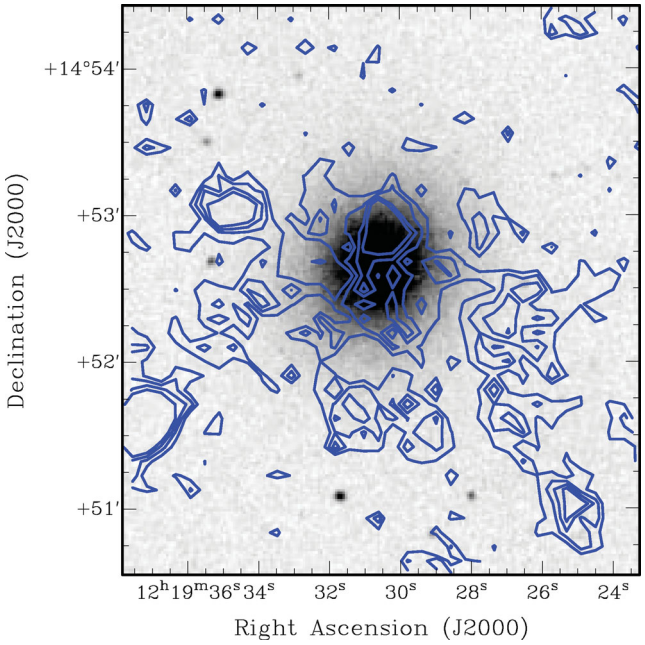

Figure 5. An example of cirrus/background contamination causing an ambiguous detection. A DSS grey-scale image overlaid with 250 μm contours at 0.005, 0.01, 0.015 and 0.02 Jy beam^{-1}. The optical centre of the target early-type galaxy, VCC 355, is offset from the peak of the 250 μm emission and the 250 μm emission is in a region of high confusion. Since the emission cannot be associated with the galaxy, it has been excluded from the catalogue.

for. The fluxes presented in Table B1 use the nominal K4 values, allowing the reader to apply the corrections separately as described in the SPIRE Observer's Manual[5] and the PACS Observer's Manual.[6] We leave the application of the correction factors to the reader, since they require prior knowledge of the extent (which can be subjective) and colour of the source. They are also tabulated in Davies et al. (2012) for a $\beta = 2$ modified blackbody.

2.4 Total uncertainty estimate

The final uncertainty measurements quoted in Table B1 consist of contributions from calibration uncertainty, $\sigma_{\rm cal}$, aperture uncertainty, $\sigma_{\rm aper}$ and zero-point uncertainty, $\sigma_{\rm zero}$. These contributions are added in quadrature thus:

$$\sigma^2_{\rm total} = \sigma^2_{\rm cal} + \sigma^2_{\rm aper} + \sigma^2_{\rm zero} \quad (1)$$

We now discuss the derivation of each of the terms in equation (1) before moving on to the verification of the *Herschel* calibration.

2.4.1 Calibration uncertainty

For SPIRE, $\sigma_{\rm cal}$ is based on scans of a single source (Neptune) and comparing it to a model of Neptune's emission. The final values for each band include a correlated 5 per cent error from the assumed model for Neptune and a 2 per cent random component from repeated measurements. The Observer's manual advises that, as a conservative measure, these values should be added together. SPIRE$\sigma_{\rm cal}$ is taken to be 7 per cent for each band.

[5] http://herschel.esac.esa.int/Docs/SPIRE/html/spire_om.html
[6] http://herschel.esac.esa.int/Docs/PACS/html/pacs_om.html

The situation is more complicated for PACS since the calibration is based on multiple sources with different models. The uncorrelated uncertainties of 3 per cent at 100 μm, 4 per cent at 160 μm and a 2.2 per cent correlated uncertainty are given for point sources, which were observed, reduced and analysed in a different way to the HeViCS PACS data. A recent technical report[7] found that PACS 160 μm data agreed with Multiband Imaging Photometer for Spitzer (MIPS) 160 μm data to within 5–20 per cent, but again, this was using two different map-making schemes to that presented here. We have erred on the side of caution and assumed a value of 12 per cent for both PACS 100 and 160 μm data, including the 2.2 per cent correlated error.

2.4.2 Aperture uncertainty

We followed the method of Ibar et al. (2010) for estimating the aperture uncertainty. We recorded the total flux within random square apertures of a given size which were laid down on the entire map. The standard deviation of these totals was measured and a 3σ cut was then applied. The standard deviation was then remeasured and a further cut applied. This was repeated until convergence and the final value of the standard deviation was taken as the aperture noise for that sized aperture. This method invariably includes a contribution from the confusion noise in the final estimate and we make no attempt to separate the confusion noise from the instrumental noise.

We combined results from individual sub-images that were used to perform the photometry, and plotted the variation of aperture noise with aperture size for each band (Fig. 6). In this plot the horizontal axis corresponds to the radii of circular apertures whose areas are equal to the square apertures described above. As a sanity check, we also performed the same analysis using the entire southernmost tile, since it has the least cirrus contamination. The entire tile was rebinned using pixels equal to the aperture size. A simple background value was subtracted based on the mean of the surrounding, rebinned pixels. Iterative sigma-clipping was then performed on the rebinned, background-subtracted image.

In all the bands, the application of aperture corrections is clearly important for objects comparable to the size of the beam. If we consider first the SPIRE data. One would expect the noise to increase $\propto n_{\rm px}^{0.5}$ for white noise, but in fact the dependence is closer to $n_{\rm px}^{0.75}$ for both the entire tile and the sub-images. At large radii, the noise measured from the sub-images exhibits a break after which the dependence is closer to the $n_{\rm px}^{0.5}$ as expected.

The difference between the noise measured from the entire tile and the noise measured from sub-images probably highlights the difference between the background estimation methods; the sub-images employ a high-order polynomial whereas for the entire tile, a simple mean is taken over a comparable area. Since the noise measured in the sub-images is closer to the expected value for Gaussian noise at large radii (although admittedly, the data are noisy), this is a good indication that the background subtraction is working well at removing background variation on these scales.

The $n_{\rm px}^{0.75}$ dependence was unexpected. At first we thought that it as probably due to the contributions from background confusion and contaminating cirrus that was poorly fit. But the same behaviour was noticed in the PACS data which has much less contamination from background sources and cirrus. Most likely, there is another source of error which is unaccounted for, perhaps from the map-making scheme itself.

[7] PICC-NHSC-TR-034

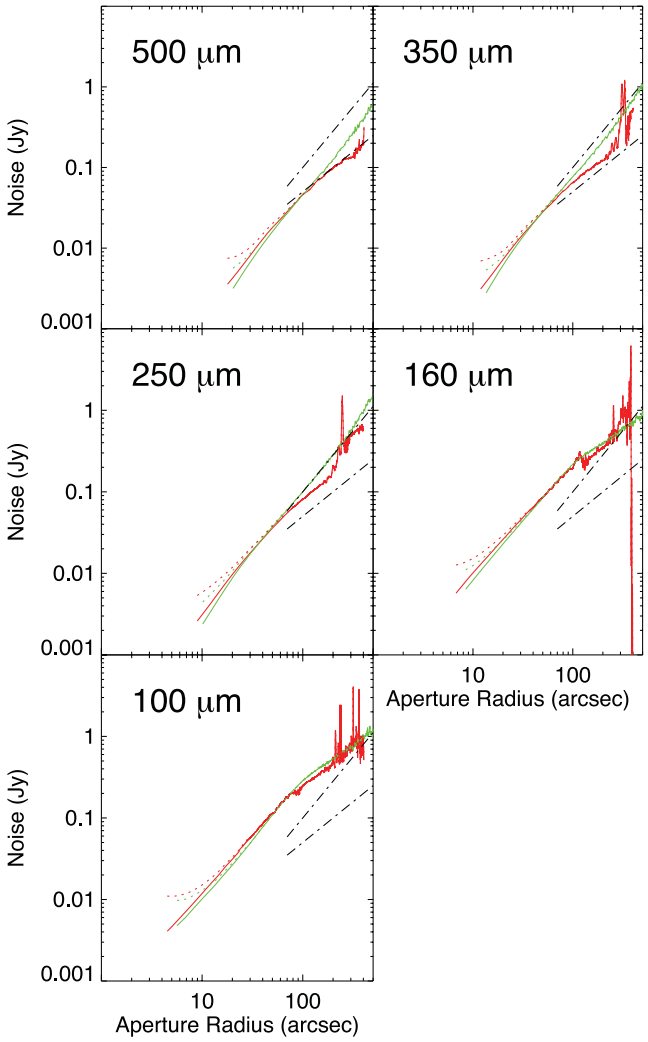

Figure 6. Variation of aperture noise with circular aperture radius. Green lines are apertures measured from the entire, full-depth region within the southern tile. Red lines show the combined results from sub-images that were extracted from the entire map to perform photometry on individual targets. Dotted lines show the same data with aperture corrections applied. Overplotted dot–dashed lines show $\sigma_{\rm aper} \propto n_{\rm px}^{0.5}$ and $\sigma_{\rm aper} \propto n_{\rm px}^{0.75}$ for comparison.

2.4.3 Zero-point error

Zero-point errors were estimated from the map of the background fit. The standard deviation of the background was measured over the extent of the source and then multiplied by the number of pixels in the source aperture. This only contributed to a significant proportion of the uncertainty for extended, low-surface brightness objects, which were rare.

2.5 Verification of flux measurements

The flux measurements from PACS were verified by comparing our measurements to previous measurements of Virgo galaxies from *ISO* 100 and 170 μm (Tuffs et al. 2002), the *IRAS* Point Source Catalogue (PSC) and the *IRAS* Faint Source Catalogue (FSC) (Moshir et al. 1993). We applied colour corrections to the PACS fluxes in accordance with the instrument team recommendations[8] in order to compare our measurements with those taken with *ISO*. When obtaining these correction factors, we assumed a blackbody temperature of 20 K, typical for dust in these galaxies (Davies et al. 2012). No colour correction is required to compare PACS 100 μm with *IRAS* 100 μm data.

A cross-match of sources yielded 46 matches from Tuffs et al. (2002), 70 from the *IRAS* PSC and 83 from the *IRAS* FSC. Although instrument-independent measurements at 250, 350 and 500 μm do not exist for the Virgo galaxies we have compared our results, which are based on an automatic measuring technique, with those of the BGS and the *Herschel* Reference Sample (Ciesla et al. 2012) which employ alternative, manual aperture photometry. For the BGS we used the original apertures but applied them to the new data sets to account for any change in flux calibration between the old data and the data presented here.

Straight-line fit parameters (with 1σ uncertainties) to the log–log plots displayed in Fig.7 are shown in Table 1. In most cases the fit values are consistent with a 1:1 correlation, to within the scatter in the residuals, so we have high confidence in the fluxes in our catalogue for which there are no previous measurements. There is a tendency to measure higher fluxes in PACS 100 μm compared to *IRAS* 100 μm data, but this tendency has already been independently identified by the instrument team and is currently under investigation. There is a notable discrepancy between our measurements and the BGS measurements of VCC 785 in the 160 μm data at ∼0.45 Jy. The immediate area surrounding the galaxy at 160 μm has significant negative flux values, and the original BGS aperture, which is based on the extent of the galaxy at 500 μm envelops these features, reducing the total flux substantially.

2.6 SED fitting

We have attempted to fit the SED for each galaxy under the assumption that the emission is entirely from thermal dust. M87 (VCC 1316), M84 (VCC 763) and NGC 4261 (VCC 345) were omitted since these galaxies have significant synchrotron emission that could potentially contaminate the SPIRE fluxes (Baes et al. 2010; Smith et al. 2012a). We employed a single-temperature modified blackbody model with a fixed emissivity index, $\beta = 2$, to fit all the galaxies for which we had flux measurements across all bands. The dust mass-opacity coefficient used was 0.192 $\rm m^2\ kg^{-1}$ at 350 μm (Draine 2003). We realize that adopting a single-temperature fit and a fixed $\beta = 2$ may be viewed as contentious in the light of recent results (e.g. Planck Collaboration et al. 2011; Boselli et al. 2012; Dale et al. 2012); however, the BGS galaxies have been shown to be well modelled by a single-temperature, $\beta = 2$ fit (Magrini et al. 2011; Davies et al. 2012). β is still a poorly understood quantity and may not even be constant within a single galaxy (Planck Collaboration et al. 2011; Smith et al. 2012b). We have chosen the simplest approach which is probably the best we can achieve with the wavelength coverage at our disposal and will provide a benchmark for future studies, which will exploit ancillary data sets to look at the effects of adopting multi-temperature, variable β models. We also acknowledge that the range of β that exists in the literature can typically lead to a factor of a few difference in the derived dust mass. This can rise to a factor of 10 if an extreme $\beta = 1$ model is assumed (Cortese et al. 2012).

[8] http://herschel.esac.esa.int/twiki/pub/Public/PacsCalibrationWeb/cc_report_v1.pdf

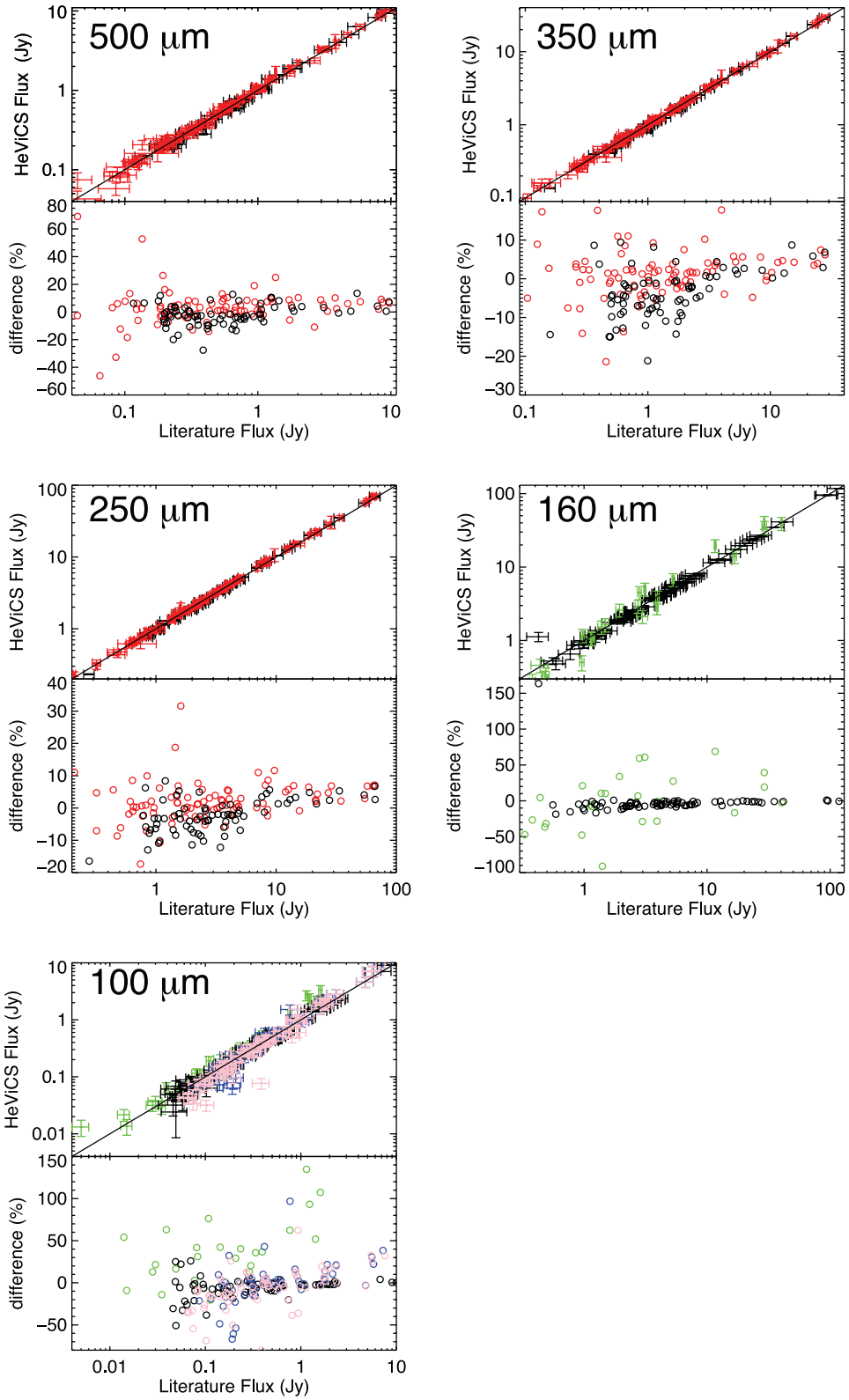

Figure 7. *Herschel* flux comparisons with *ISO* (green open circles), *IRAS* Point Source Catalogue (blue open circles), *IRAS* Faint Source Catalogue (pink open circles), the HeViCS BGS (open black circles) and the *Herschel* reference sample (open red circles). Top left: 500 μm; top right: 350 μm; middle left: 250 μm; middle right: 160 μm; and bottom left: 100 μm. The 1:1 fit lines is shown in black, see text for details of individual fits to the plots. The percentage difference between HeViCS and the literature values is given below each plot. The outlier at 160 μm is VCC 785 (see text for further details).

Table 1. Linear fit parameters to comparisons of *Herschel* fluxes with literature values. Uncertainties are shown in parentheses.

Wavelength (μm)	Gradient	Intercept	Scatter
100[a]	0.97 (0.02)	−0.03 (0.02)	0.08
100[b]	1.02 (0.04)	0.16 (0.03)	0.13
100[c]	1.11 (0.02)	−0.08 (0.02)	0.05
100[d]	1.11 (0.02)	−0.09 (0.02)	0.08
160[a]	1.041 (0.006)	−0.048 (0.006)	0.02
160/170[b]	1.08 (0.04)	−0.01 (0.03)	0.13
250[a]	1.012 (0.004)	−0.006 (0.003)	0.02
250[e]	0.997 (0.004)	0.020 (0.003)	0.02
350[a]	1.015 (0.006)	−0.012 (0.003)	0.02
350[e]	0.989 (0.004)	0.017 (0.003)	0.02
500[a]	0.994 (0.007)	0.009 (0.006)	0.03
500[e]	0.98 (0.01)	0.028 (0.005)	0.03

[a]BGS (Davies et al. 2012).
[b]*ISO* (Tuffs et al. 2002).
[c]*IRAS* PSC.
[d]*IRAS* FSC.
[e]HRS (Ciesla et al. 2012).

The SED-fitting algorithm works by minimizing the difference between the set of measured fluxes and a set of model fluxes at the same wavelengths. The model fluxes are generated by taking a modified blackbody function and multiplying it by the *Herschel* filter profiles. This step requires measured fluxes that have had the original K4 scaling factor removed. A simplex technique is used to find the most likely combination of temperature and mass and several thousand Monte Carlo simulations are then employed to derive the error distributions for the dust mass and temperature. These simulations lend a greater degree of robustness over simpler χ^2-minimizing algorithms which might assume that the error distributions are Gaussian. The method also takes into account uncorrelated calibration uncertainties for SPIRE and PACS (see Section 2.2 for these values) and correlated calibration errors between SPIRE bands which are of the order of 5 per cent. The results of the Monte Carlo simulations indicated that the errors in dust mass and temperature are anticorrelated, but are centred on the correct values (see Smith et al. 2012b).

In order to estimate the dust mass, it was necessary to provide an estimate for the distance. We have adopted the distances provided by GOLDMINE which quote the average distance to the subcluster to which each individual galaxy belongs, as measured in Gavazzi et al. (1999).

In some cases it was clear, both from the χ^2 values and from visual inspection of the fits that a single-temperature fit was an inappropriate choice. We have not attempted further modelling of these galaxies since future papers will examine multi-temperature models, employing variable β, with the help of additional data sets which will provide the necessary extra wavelength coverage to better constrain the more complex models (Grossi et al., in preparation).

3 RESULTS

3.1 Detection rates

Table2 displays the detection rates for the entire 84 deg^2 region and the inner 55 deg^2 covered to optimum depth. In this table we have included all galaxies that yielded a detection at 250 μm. The breakdown of the FIR detections by m_{pg} for each wavelength are shown in Fig.8 (top row) for the two survey regions. Surprisingly there does not appear to be any significant decrease in detection rates in the regions with less coverage. This is probably suggesting that *Herschel* is sensitive enough to detect all the FIR-emitting Virgo galaxies within a couple of passes. Individual fluxes for each galaxy can be found in Table B1.

Table 2. *Herschel* detection rates of VCC galaxies contained within the HeViCS survey limits. Results are given for the whole survey region and the inner region covered to full depth.

Wavelength (μm)	Entire survey region (84 deg^2) (750 objects)	Eight-scan survey region (inner 55 deg^2) (602 objects)
500	204 (27 per cent)	160 (27 per cent)
350	232 (31 per cent)	184 (31 per cent)
250	254 (34 per cent)	203 (34 per cent)
160	210 (28 per cent)	176 (29 per cent)
100	195 (26 per cent)	165 (27 per cent)

The difference between FIR detections (predominantly thermal dust) and optical detections is evident at low optical luminosities in Figs 8 and 9. The galaxy cluster population is dominated by low-luminosity dwarfs, in particular dEs, but few of these galaxies are detected in FIR. Since these galaxies are deficient in dust, it is unsurprising that their detection rates are low. This is also demonstrated in Fig. 8(b), which displays the same information but broken down by galaxy type. The other early types also have low detection rates, as these too have little dust present in the ISM. The late types have high detection rates in both PACS and SPIRE as one would expect since these galaxies are rich in dust.

Fig. 9 shows the morphology–magnitude plot, highlighting detected and undetected galaxies. This plot allows us to compare different galaxy morphologies at the same optical magnitude. From this it is clear that the lack of FIR detections of dEs, ellipticals (Es) and irregulars (Im/S) is not simply because they are faint at optical magnitudes – there are many FIR non-detections which have an optical magnitude greater than the faintest detection.

The Magellanic-type dwarfs are notable by their lack of detection rates amongst the late types. Although these systems are metal poor and would not necessarily be expected to contain much dust, they are of similar metallicity to the blue compact dwarfs (BCDs), which have a higher detection rate. This suggests that the lack of Sm/Im galaxies is more than likely due to these galaxies falling below the surface brightness detection threshold.

Although the early types are more readily detected in the optical compared to the FIR, the bins are by no means empty as one might expect of a population of dust-deficient systems. These exceptional galaxies have been the focus of previous HeViCS studies (e.g. de Looze et al. 2010; Grossi et al. 2010; Smith et al. 2012a) and will be the subject of future analyses as these new data are fully exploited (di Serego Alighieri, in preparation; Grossi et al., in preparation).

3.2 Background contamination

As explained in Section 2.3, during the formation of the catalogue, some FIR detections were rejected either because the FIR emission did not coincide with a foreground optical galaxy, or could not be distinguished from the surrounding cirrus. Despite the precautions taken to avoid contamination from background sources, there is still a possibility of accidentally reporting the flux from a background galaxy.

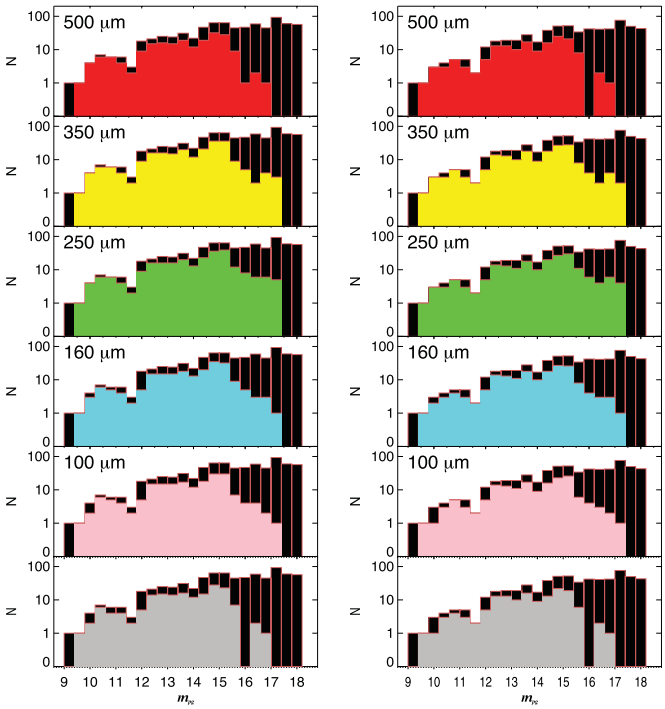

(a) Distribution of FIR detections sorted by photographic apparent magnitude, m_{pg}.

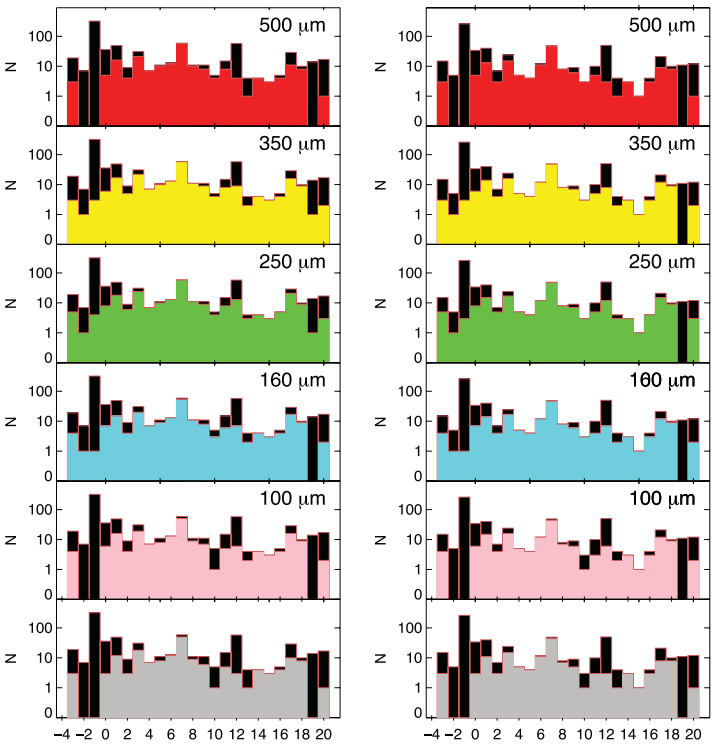

(b) FIR detections sorted by morphological type.

Figure 8. FIR detections for the VCC galaxies: (a) distribution of FIR detections sorted by photographic apparent magnitude, $m_{\rm pg}$; (b) FIR detections sorted by morphological type. The left-hand panels correspond to the entire survey region (84 deg^2), the right-hand panels correspond to the central 55 deg^2 with optimum coverage. Black represents the optical detections of the VCC galaxies down to the completeness limit, $m_{\rm pg} \leq 18$. 500, 350, 250, 160, 100 μm and five-band detections are represented by red, yellow, green, cyan, pink and grey histograms, respectively. Galaxy morphology is as follows: **−3**: dS0, **−2**: dE/dS0, **−1**: dE (d:E), **0**: E–E/S0, **1**: S0, **2**: S0a–S0/Sa, **3**: Sa, **4**: Sab, **5**: Sb, **6**: Sbc, **7**: Sc (dSc), **8**: Scd, **9**: Sd, **10**: Sdm–Sd/Sm, **11**: Sm, **12**: Im (Im/S), **13**: Pec, **14**: S/BCD (dS/BCD dS0/BCD Sd/BCD), **15**: Sm/BCD, **16**: Im/BCD, **17**: BCD, **18**: S (dS), **19**: dIm/dE and **20**: ?

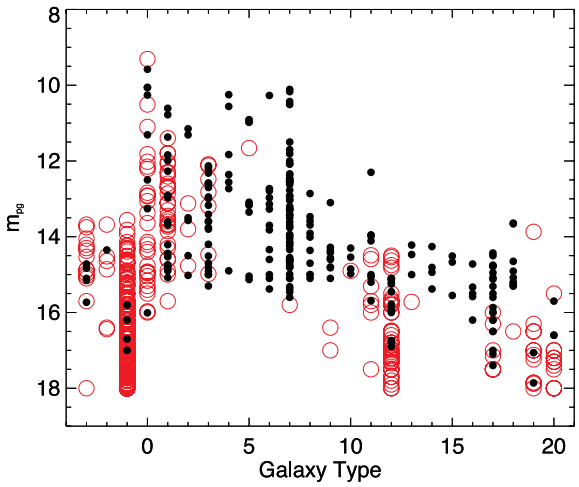

Figure 9. Morphology–magnitude plot for the VCC sample within the entire HeViCS area. Galaxies with a detection in at least one band are black solid circles, while undetected galaxies are open red circles. Galaxy morphology numbering follows that in Fig. 8.

In order to estimate this effect, we have adopted a naïve approach. We restricted the analysis to the total population of point sources and undetected sources. Extended sources at the expected positions of Virgo galaxies can be reliably attributed to those galaxies. We then assumed that the background galaxy population is randomly distributed on the sky and worked out the probability of a chance alignment within each SPIRE beam, based on the source counts of Glenn et al. (2010). This probability is then used to predict the number of possible spurious sources in the catalogue in different flux bins.

If one has chosen the rejected galaxies wisely, then one would expect that the number of spurious measurements should be approximately equal to the predicted number of contaminating background sources. In Table3 we show the results of this test. From this table we see that at 500 μm the number of rejections is approximately equal to the number of predicted sources. At 350 and 250 μm, we appear to have been overzealous in excising galaxies at the lowest fluxes. We attribute at least some of the increase in the number of spurious detections to peaks in the cirrus, which are expected at these low fluxes. Above 45 mJy the number of rejected sources compares well with the predictions.

The agreement between the number of spurious sources and the number of predicted background sources does not guarantee that the correct set of galaxies has been selected in the catalogue. However, the fact that the selection was made by comparing FIR emission with optical data does provide a greater degree of reliability. The combination of these points suggests that it is likely that none of the catalogue has been misidentified.

3.3 FIR colours

Recently, Boselli et al. (2012) examined SPIRE colours for the Herschel Reference Sample (HRS) sample of 322 nearby galaxies. They observed a number of trends between FIR colour, metallicity, star formation history, the ionizing radiation field and surface brightness. They also used the SPIRE only colours to argue that when fitting a fixed emissivity index, single-temperature modified blackbody model to the FIR SED, $\beta = 2$, is inappropriate for all but the most metal-rich, high surface brightness galaxies in the HRS. However, due to the degeneracy between temperature and β, SPIRE-only colours are not adequate to constrain β. We demonstrate this with Figs 10(a) and (b) which compare SPIRE only colours with SPIRE-PACS colours.

Table 3. Estimates of contamination from background galaxies in the SPIRE bands. N_a is the number of sources that were accepted into the catalogue, N_r is the number of sources that were rejected as spurious and N_p is the number density of sources predicted from the number counts of Glenn et al. (2010). Contamination is the expected percentage contamination based on the source counts. N_c is the expected number of contaminating sources.

Flux bin (mJy)	N_a	N_r	N_p (deg^{-2})	Contamination (per cent)	N_c
250 μm					
15–20	8	47	1694	5.5	28
20–45	20	41	1824	5.9	31
45–100	6	6	313	1	5
100+	4	1	25	0.08	0
350 μm					
17–20	1	27	566	3	17
20–45	20	55	1209	7	38
45–100	6	4	154	0.9	5
100+	4	1	73	0.3	1.6
500 μm					
17–20	3	14	185	2	11
20–45	29	45	614	7	41
45–100	3	2	19	0.2	1
100+	2	0	1	0.01	0

The fluxes that were used to create these figures were derived using the fluxes from Table B1, and dividing out the K_4 factor. This provides us with a set of instrumental fluxes that have been corrected for the size of the aperture, with no assumption on spectral index. We then generated a set of ideal modified blackbody functions with varying β and temperatures. These models were multiplied by the instrument filter functions to reproduce the instrumental fluxes for each band. The black filled squares in Figs 10(a) and (b) represent the theoretical colours derived from these model instrumental fluxes. Loci joining models of constant β but variable temperature were then overplotted (black lines).

Grey bars indicate the uncertainty in each colour. These have been derived by adding the relative flux uncertainties in quadrature for a given colour. Since colours common to one instrument are unaffected by correlated uncertainties, we have removed the 5 per cent correlated error, when deriving the SPIRE, $S250/S500$ colour uncertainty.

A comparison of Fig. 10(a) with Boselli et al. (2012) fig. 9 shows that the galaxies in HeViCS exhibit similar trends in SPIRE colours to those in the HRS. There appears to be two clusters of objects around the $\beta = 1.5$ line and $\beta = 1$, but the uncertainties in the colours prevent one from disentangling the temperature-β degeneracy. So the cluster of galaxies around ($\beta = 1$, $T = 30$ K) could also be consistent with a ($\beta = 2$, $T = 17$ K) model.

The situation improves when a PACS colour is introduced (Fig. 10b). It is easier to distinguish between different models of β and T, and we are able to constrain the temperature with much greater accuracy. We now see that the HeViCS galaxies exhibit a range of β from 1–2 and the cold ($T < 15$K) galaxies are unambiguously cold. Most of the galaxies appear to cluster around the models corresponding to $\beta = 1.5$ and 2 with temperatures varying between 20 and 30 K. This is very similar to the β, T distributions

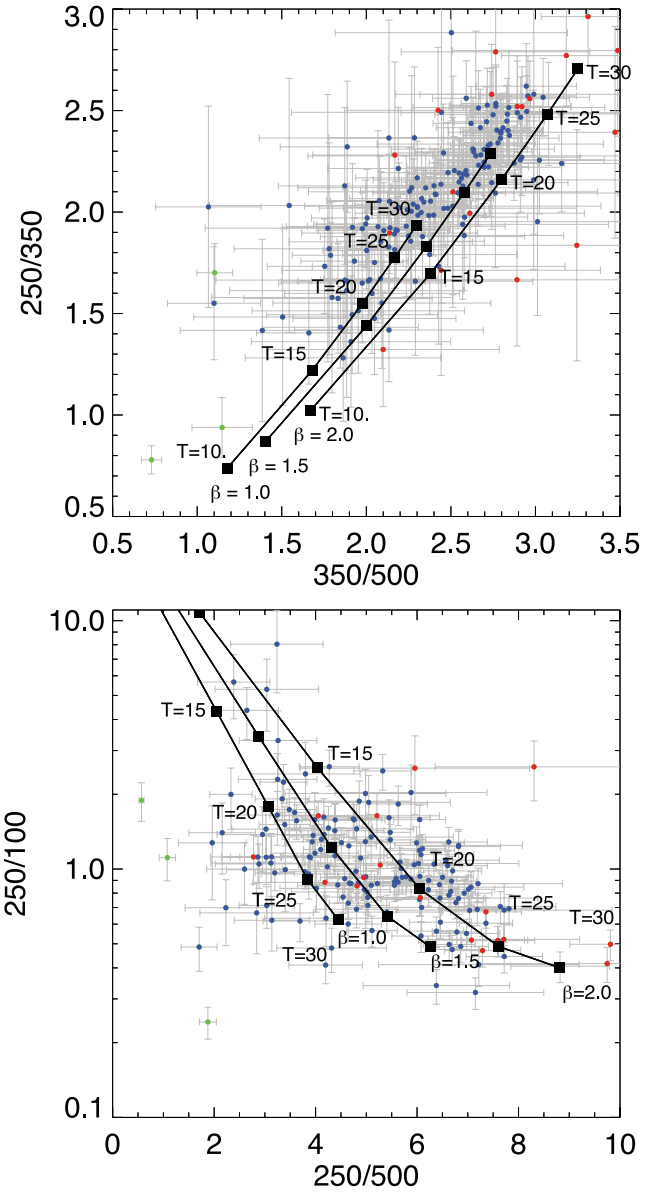

Figure 10. Colour–colour plots for the entire HeViCS catalogue detected in all bands. Blue points are late types, red points are early types and green points are galaxies known to harbour AGN. Loci connecting models of constant β, but variable temperature are overplotted in black, with different temperatures labelled every 5 K.

observed by Dunne & Eales (2001) and typical of values used in the literature (Magnelli et al. 2010; Dunne et al. 2011; Skibba et al. 2011; Davies et al. 2012; Roseboom et al. 2012; Smith et al. 2012a).

There is also a cluster of objects that are consistent with $\beta = 1$ models. Values of β as low as one are often observed in individual regions within the Milky Way (Dupac et al. 2003; Bracco et al. 2011) but are rarely seen in the SEDs of galaxies which are integrated over the whole galaxy. This region of the colour–colour plot becomes increasingly sensitive to contributions from either synchrotron or free–free emission (which would boost the 500 μm relative to the 250 μm), and warmer dust (which would boost the 100 μm relative to the 250 μm). The known AGN have the reddest colours but surprisingly we find a late-type, VCC 223, in amongst them. An analysis of the SED reveals that it has a high 500 μm flux relative to the other bands. This excess could be due to free–free or synchrotron

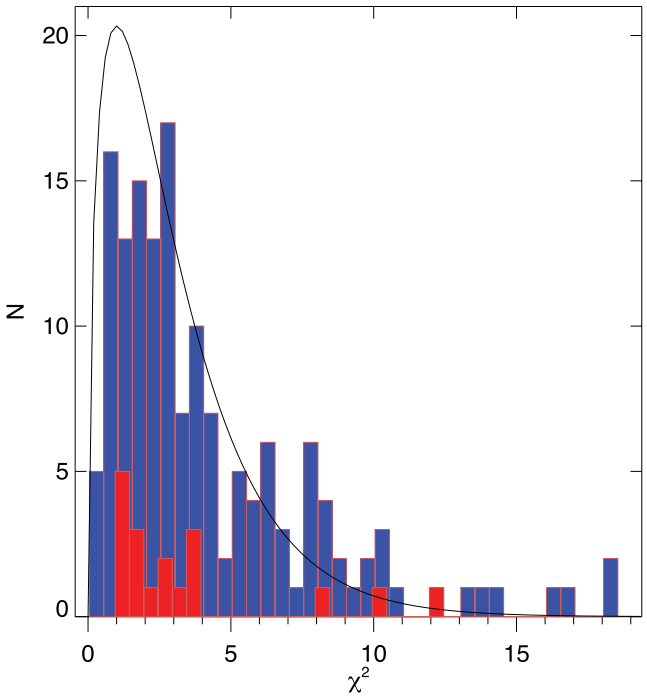

Figure 11. χ^2 distribution from single-temperature, modified blackbody model fits for 161 HeViCS galaxies with five-band photometry. Early-type galaxies are shown in red, and late-type galaxies are shown in blue. Overplotted is the theoretical χ^2 distribution for 168 galaxies, assuming 3 degrees of freedom.

emission from recent star formation as this galaxy is classed as a BCD. However, we cannot rule out the possibility that this galaxy harbours a very cold dust component.

With such a large spread in the values of β implied by the data, it is a useful exercise to explore the validity of a single-temperature, fixed-beta modified blackbody model, which are commonly used throughout the literature.

3.4 SED fits, dust masses and temperatures

We restricted our analysis of the SEDs to 168 of the 171 galaxies which were detected in all five bands of PACS and SPIRE. M87, M84 and NGC 4261 were omitted since their SEDs contain significant synchrotron emission and they, along with the other early-type VCC galaxies, will be the focus of a forthcoming paper (di Serego Alighieri et al., in preparation). The distribution of χ^2 for the 168 galaxies is shown in Fig. 11. For 140 galaxies the single-temperature model produced an adequate fit ($\chi^2_{\mathrm{d.o.f.}=3} < 7.8$, at a confidence level of 95 per cent) so that no further fitting was required. For the remaining 28 galaxies, the single-temperature model was unsuitable. This number of galaxies is significantly larger than the ∼8 (5 per cent) expected from the χ^2 distribution for three degrees of freedom, providing quantitative evidence that the single-temperature, $\beta = 2$ model is not appropriate for the FIR SEDs of all of these galaxies. Modelling of different dust populations will be studied in a future paper.

Out of the 429 early-type galaxies in the VCC that are located inside the HeViCS field, only 15 meet the requirement of $\chi^2_{\mathrm{d.o.f.}=3} < 7.8$. This should be kept in mind in the following simple analysis since these galaxies are clearly unusual for their type. Dust masses and temperatures are recorded in Table C1. On inspection, the upper and lower limits for the dust mass and temperature were symmetric

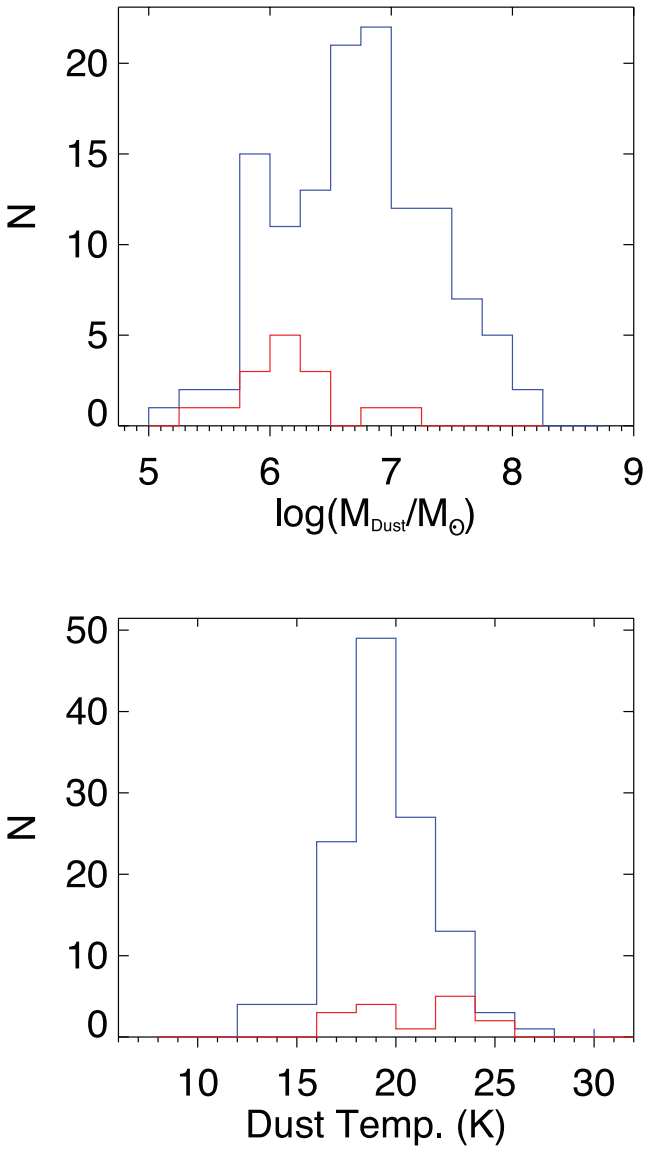

Figure 12. Temperature and mass distributions split by galaxy type. Blue columns represent types Sa and later, red represents types earlier than Sa. Only galaxies whose model fits have $\chi^2 < 7.8$ are included.

to one significant figure, so we have just quoted one value. The SEDs are shown in Fig. D1. The χ^2 for each fit is recorded at the top of each plot.

In Fig. 12 we show the distributions of dust mass and temperature that were derived from our SED fits, using only the 140 galaxies with a $\chi^2 < 7.8$ from the single-temperature modified blackbody spectrum model fitting. Each plot shows the different distributions based on galaxy type; types earlier than Sa are shown in red outline, while types Sa and later are shown in blue.

The late types exhibit a range in dust mass of $\log(M_{\rm dust}/{\rm M}_\odot)$ =5.2–8.1, with a mean value of $\log[\langle M_{\rm dust}\rangle/{\rm M}_\odot]$ = 7.1 ± 0.1. In contrast, the early types exhibit a narrower range of masses; $\log(M_{\rm dust}/{\rm M}_\odot)$ =5.4–7.0, with a lower mean value of $\log[\langle M_{\rm dust}\rangle/{\rm M}_\odot]$ = 6.3 ± 0.3. For the temperature distributions, the late types range from 12.9 to 26.4 K, with a mean value of $\langle T\rangle$ = 19.4 ± 0.2 K. The early types cover a range in temperature from 16.2 to 25.9 K, with a mean value, $\langle T\rangle$ = 21.1 ± 0.8 K. A comparison of the dust properties of the late types is consistent with those from the BGS. This is not surprising, since the BGS consisted of the brightest FIR/submm galaxies in HeViCS, which are mostly late-type galaxies.

We performed a Kolmogorov–Smirnov (KS) two-sample test, Mann–Whitney *U*-test and an *F*-test to look for significant differences between the two sample populations and in addition, compared the two samples to their equivalent samples in the HRS (Cortese et al. 2012; Smith et al. 2012a). We note here that the HeViCS sample probes lower mass galaxies than those in the HRS, which may slightly bias the results. The late-type comparison is limited to the mass distribution since Cortese et al. (2012) did not attempt to estimate dust temperatures for their sample.

The results of the tests are displayed in Table 4 , and show that there is a clear distinction between the dust masses and temperatures of cluster late types and cluster early types: Virgo late-type galaxies have typically cooler, and more massive dust reservoirs than Virgo early types. The tests also imply that late types in the field have a significantly different mass distribution to those in the cluster. The effect of the cluster environment on the bulk dust properties of the early types is much less pronounced, with the tests revealing a fairly high probability that the cluster and field samples were drawn from the same distribution. Since the early types are dominated by S0 galaxies in both samples, this is suggesting that the bulk dust properties of S0s are the same inside and outside the cluster. However, as noted in Cortese et al. (2012), differences in the dust properties may be more noticeable if the samples are defined on a property that is more indicative of a galaxy undergoing an interaction with the cluster (e.g. H I deficiency) rather than cluster membership alone.

One aspect of recent *Herschel* galactic studies that has provoked keen interest in the wider community is the existence of galaxies that seem to possess an excess of emission at 500 μm (e.g. Grossi et al. 2010; Galametz et al. 2011; Dale et al. 2012) so it would seem pertinent to comment on their presence in the catalogue. Such galaxies are interesting because there is still disagreement on the origin of the excess. The excess could be due to an as yet undiscovered very cold dust component, thermal free–free emission, synchrotron

Table 4. Virgo cluster and field comparisons of the dust mass and temperature distributions of early- and late-type galaxies.

Comparison samples		μ_1	σ_1	μ_2	σ_2	KS test		MW *U*-test		*F*-test	
1	2					Value	$p_{\rm value}$	Value	$p_{\rm value}$	Value	$p_{\rm value}$
Dust mass [$\log(M_{\rm dust}/{\rm M}_\odot)$]											
Cluster late	Cluster early	7.1	1.6	6.3	1.2	0.52	0.0007	−3.48	0.0002	64.27	10^{-10}
Cluster late	Field late	7.1	1.6	7.3	1.6	0.33	9×10^{-7}	4.82	7×10^{-7}	2.58	10^{-7}
Cluster early	Field early	6.3	1.2	6.6	1.2	0.29	0.45	0.67	0.25	2.61	0.08
Dust temperature (K)											
Cluster late	Cluster early	19.4	2.5	21.1	3.2	0.34	0.06	1.82	0.035	1.7	0.14
Cluster early	Field early	21.1	3.2	23.5	4.6	0.31	0.37	1.50	0.07	2.06	0.18

emission or something more exotic (e.g. spinning dust; Bot et al. 2010).

We have defined the excess as those galaxies whose 500 μm flux is at least 2σ above the model fit. This yields six candidates (VCC 120, VCC 223, VCC 562, VCC 848, VCC 971 and VCC 1673) with an excess at 500 μm. VCC 1673 is discounted because of the contamination from VCC 1676. VCC 971 (NGC 4423) is an Sd; VCC 223, VCC 562 and VCC 848 are BCDs and VCC 120 is classed as an Scd. We prefer not to speculate, at this point, as to the source of this excess, merely to highlight these objects as interesting. This is partly because six galaxies is about the amount of galaxies expected to be 2σ outliers, but even if the deviations have non-statistical origins, we do not have sufficient wavelength coverage in this data set to be able to constrain more complex SEDs which might account for the excess.

There is currently a HeViCS observing program with PACS at 70 μm which should help constrain the SED at the shorter wavelengths for a substantial sample of the Virgo galaxies displayed here. In addition to this, the recent work of Bendo, Galliano & Madden (2012) will provide *Spitzer*-MIPS photometry (24, 70 and 160 μm) for a significant fraction of the VCC galaxies. The combination of these two data sets will constrain the warmer (>30 K) dust component, while ongoing millimetre observations and archived radio observations of the emerging population showing 500 μm excess, should be able to provide the necessary spectral coverage to constrain the longer wavelengths and ascertain the origin of the excess.

4 SUMMARY

We have undertaken the largest and deepest survey of the Virgo cluster at FIR wavelengths with the *Herschel Space Observatory*, utilizing both PACS and SPIRE instruments. The survey, which is now complete in five FIR bands, covers 84 $\deg^2$ of the Virgo cluster encompassing 750 VCC galaxies brighter than the optical completeness limit. We recover 254 (34 per cent) of the VCC population in at least one wavelength and have five-band FIR photometry for 171 galaxies. The photometry compares well with previous surveys showing typically less than a 10 per cent variation across all bands.

FIR colours from PACS and SPIRE have been compared to model single-temperature modified blackbody spectra incorporating a fixed emissivity index. The distribution of colours is consistent with a range of $\beta = 1$–2. This is supported by a study of the χ^2 distribution from $\beta = 2$ model fits to the galaxies with five-band photometry. The amount of galaxies, not well fitted by the model, is too large to be explained by random fluctuations. Further modelling is required to explore variable beta and/or different dust temperature populations, although this will likely require more measurements at FIR/MIR and submm wavelengths to be properly constrained.

A preliminary analysis of different morphological types indicates that dust in Virgo early types has the same temperature and mass distribution as early types in the field, suggesting that the environment has little impact on their bulk dust properties. Since the early types are dominated by S0s, it suggests that the processes responsible for creating S0s have taken place before they enter the cluster. In contrast, the late types have significantly different mass and temperatures to those in the field.

As well as providing a table of flux measurements and images of FIR SEDs with this manuscript, we will be providing the community with a legacy product which consists not only of the final 84 $\deg^2$ maps but also detailed data products such as cut-outs of the fully processed images for each galaxy, the intermediate products that were used in the measurement process and the resulting radial profiles in each band. These will ensure the legacy value of the HeViCS.

ACKNOWLEDGMENTS

We would like to thank the anonymous referee for his/her helpful comments and suggestions for improving this manuscript.

SPIRE has been developed by a consortium of institutes led by Cardiff University (UK) and including University of Lethbridge (Canada); NAOC (China); CEA, LAM (France); IFSI, University of Padua (Italy); IAC (Spain); Stockholm Observatory (Sweden); Imperial College London, RAL, UCL-MSSL, UKATC, University of Sussex (UK); and Caltech, JPL, NHSC, University of Colorado (USA). This development has been supported by national funding agencies: CSA (Canada); NAOC (China); CEA, CNES, CNRS (France); ASI (Italy); MCINN (Spain); SNSB (Sweden); STFC (UK); and NASA (USA). HIPE is a joint development (are joint developments) by the Herschel Science Ground Segment Consortium, consisting of ESA, the NASA Herschel Science Center, and the HIFI, PACS and SPIRE consortia.

This research has made use of the GOLDMINE Database, operated by the Università degli Studi di Milano-Bicocca

The research leading to these results has received funding from the European Community's Seventh Framework Programme (/FP7/2007–2013/) under grant agreement No. 229517.

REFERENCES

Abadi M. G., Moore B., Bower R. G., 1999, MNRAS, 308, 947
Alton P. B., Bianchi S., Rand R. J., Xilouris E. M., Davies J. I, Trewhella M., 1998, A&A, 335, 807
Baes M. et al., 2010, A&A, 518, L53
Bendo G. J., Galliano F., Madden S. C., 2012, MNRAS, 423, 197
Binggeli B., Sandage A., Tammann G. A., 1985, AJ, 90, 1681
Binggeli B., Popescu C. C., Tammann G. A., 1993, A&AS, 98, 275
Boselli A., Gavazzi G., 2006, PASP, 118, 517
Boselli A. et al., 2012, A&A, 540, A54
Bot C., Ysard N., Paradis D., Bernard J. P., Lagache G., Israel F. P., Wall W. F., 2010, A&A, 523, A20
Bracco A. et al., 2011, MNRAS, 412, 1151
Chapin E. L. et al., 2011, MNRAS, 411, 505
Ciesla L. et al., 2012, A&A, 543, 161
Clemens M. S. et al., 2010, A&A, 518, L50
Corbelli E. et al., 2012, A&A, 542, A32
Cortese L. et al., 2010, A&A, 518, L49
Cortese L. et al., 2012, A&A, 540, A52
Côté P. et al., 2004, ApJS, 153, 223
Dale D. A. et al., 2012, ApJ, 745, 95
Davies J. I. et al., 2010, A&A, 518, L48
Davies J. I. et al., 2012, MNRAS, 419, 3505
de Looze I. et al., 2010, A&A, 518, L54
de Vaucouleurs G., 1961, ApJS, 6, 213
Devereux N. A., Young J. S., 1990, ApJ, 359, 42
Dowell C. D. et al., 2010, in Oschmann J. M. Jr., Clampin M. C., MacEwen H. A., eds, Proc. SPIE Vol. 7731, Space Telescopes and Instrumentation 2010: Optical, Infrared, and Millimeter Wave. SPIE, Bellingham, p. 773136
Draine B. T., 2003, ARA&A, 41, 241
Dunne L., Eales S. A., 2001, MNRAS, 327, 697
Dunne L., Eales S. A., 2002, Ap&SS, 281, 321
Dunne L. et al., 2011, MNRAS, 417, 1510
Dupac X. et al., 2003, A&A, 404, L11
Ferrarese L., 2011, in Fornax, Virgo, Coma et al.: Stellar Systems in High Density Environments. ESO, Garching

Galametz M., Madden S. C., Galliano F., Hony S., Bendo G. J., Sauvage M., 2011, A&A, 532, A56
Gavazzi G., Boselli A., Scodeggio M., Pierini D., Belsole E., 1999, MNRAS, 304, 595
Gavazzi G., Boselli A., Donati A., Franzetti P., Scodeggio M., 2003, A&A, 400, 451
Gavazzi G. et al., 2008, A&A, 482, 43
Glenn J. et al., 2010, MNRAS, 409, 109
Gomez H. L. et al., 2010, A&A, 518, L45
Griffin M. J. et al., 2010, A&A, 518, L3
Grossi M. et al., 2010, A&A, 518, L52
Gunn J. E., Gott J. R., III, 1972, ApJ, 176, 1
Ibar E. et al., 2010, MNRAS, 409, 38
Kennicutt R. C., Jr et al., 2003, PASP, 115, 928
Kim S., Rey S.-C., Sung E.-C., Yi W., Lisker T., 2011, in Koleva M., Prugniel P., Vauglin I., eds, EAS Publ. Ser. Vol. 48, New Catalog and Ultraviolet Properties of Dwarf Galaxies in the Virgo Cluster. EDP Sciences, p. 71
Magnelli B. et al., 2010, A&A, 518, L28
Magrini L. et al., 2011, A&A, 535, A13
Marsden G. et al., 2009, ApJ, 707, 1729
Mei S. et al., 2010, in American Astron. Soc. Meeting Abstracts 215, Vol. 42, The Next Generation Virgo Cluster Survey. American Astronomical Society, p. 470.05
Merritt D., 1984, ApJ, 276, 26
Mihos J. C., 2004, in Mulchaey J. S., Dressler A., Oemler A., eds, Clusters of Galaxies: Probes of Cosmological Structure and Galaxy Evolution, p. 277
Mihos J. C., Harding P., Feldmeier J., Morrison H., 2005, ApJ, 631, L41
Moore B., Katz N., Lake G., Dressler A., Oemler A., 1996, Nat, 379, 613
Moshir M. et al., 1993, VizieR Online Data Catalog, 2156, 0
Nguyen H. T. et al., 2010, A&A, 518, L5
Oosterloo T., van Gorkom J., 2005, A&A, 437, L19
Pappalardo C. et al., 2012, A&A, 545, 75
Planck Collaboration, Ade P. A. R. et al., 2011, A&A, 536, A17
Poglitsch A. et al., 2010, A&A, 518, L2
Pohlen M. et al., 2010, A&A, 518, L72
Popescu C. C., Tuffs R. J., Völk H. J., Pierini D., Madore B. F., 2002, ApJ, 567, 221
Roseboom I. G. et al., 2012, MNRAS, 419, 2758
Skibba R. A. et al., 2011, ApJ, 738, 89
Smith M. W. L. et al., 2010, A&A, 518, L51
Smith M. W. L. et al., 2012a, ApJ, 748, 123
Smith M. W. L. et al., 2012b, ApJ, 756, 40
Tuffs R. J. et al., 2002, ApJS, 139, 37
Vollmer B., Cayatte V., Balkowski C., Duschl W. J., 2001, ApJ, 561, 708

APPENDIX A: MODELLING THE GALAXY PAIR NGC 4567/8 (VCC 1673/6)

The interaction between NGC 4567 and NGC 4568 gives rise to a region of FIR emission consisting of contributions from each galaxy. Fig.A1(a) shows the 250 μmmap of the region with the d_{25} ellipses outlined. A mask was constructed from the 250 μm data to isolate the emission from only NGC 4567 (Fig. A1 b). This galaxy was chosen because it is the fainter of the two. Since it is fainter, any error in the NGC 4567 model will have less impact on the flux estimate in the overlapping region than attempting to model NGC 4568.

The ellipse fitting procedure described in Section 2.2 was applied to the masked 250 μm image. The procedure was manually limited to an extent of 2 arcmin – the minimum distance to cover the overlapping region. The model was then constructed in two parts; for the region containing emission from only NGC 4567, the original map data were used, for the overlap region, the surface brightness values from the ellipse fitting were used (Fig. A1c).

The model was then subtracted from the original map, to produce a map with only the estimated flux from NGC 4568. An aperture was defined to encompass both galaxies in the original map to enable us to measure the total flux for both galaxies combined. Care was also taken to exclude bright background galaxies from this aperture. The same aperture was then used to measure the estimated flux of NGC 4568 in the model-subtracted map (Fig. A1d).

The estimate of the flux in NGC 4567 was then simply taken as the difference of the two measurements. The procedure was then repeated using the 250 μm mask and aperture as the templates for the other bands. The resulting fluxes are very similar to the BGS values which employed a simple spatial cut between galaxies to define the extent of each. This is probably because the emission in the overlap region is dominated by NGC 4568. We have adopted a conservative estimate for the flux measurement uncertainty of 20 per cent across all bands.

APPENDIX B: TABLE OF FIR FLUXES AND UPPER LIMITS FOR 750 VCC GALAXIES IN THE HEVICS FIELD

APPENDIX C: TABLE OF DUST MASSES AND TEMPERATURE DERIVED FROM SINGLE-TEMPERATURE MODIFIED BLACKBODY FITS TO 140 VCC GALAXIES

APPENDIX D: FIR SED PLOTS WITH SINGLE-TEMPERATURE MODIFIED BLACKBODY FITS

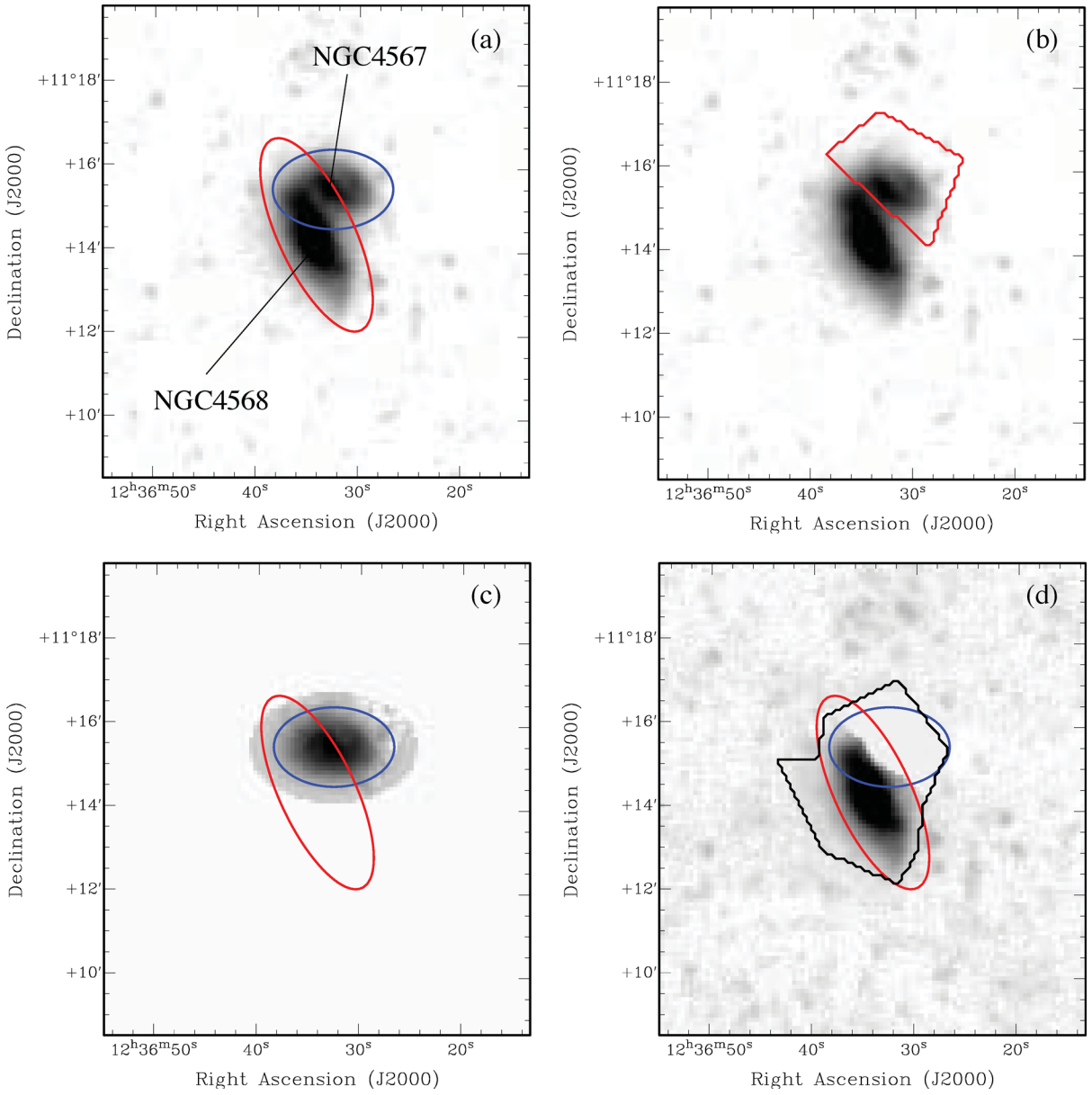

Figure A1. Images of the modelling process for galaxy pair NGC 4567/8. Log flux scales have been employed to enhance the bright and dim features. (a) 250 μm grey-scale image showing the two galaxies and their optical extent measured to d_{25}. (b) Isolated emission from NGC 4567 (red outline) was used to create a mask. (c) The model of NGC 4567. (d) The model-subtracted image showing only the emission from NGC 4568. The aperture that was used to measure the total flux of the system is shown outlined in black.

Table B1. Example table of five-band FIR detections and upper limits for the VCC galaxies (the complete table is available in the online version of this paper; see Supporting Information). Uncertainties on detections are the quadrature sum of the aperture noise and the calibration uncertainty (as described in Section 2.2). Where galaxies are listed undetected, upper limits are given in the error column and are defined as the 3σ upper limit, measured from the PSF-convolved map. Galaxies that fell outside of the PACS footprint are unmeasured at 160 and 100 μm. Asterisks denote galaxy measurements that were confused by foreground cirrus or unresolved background sources. VCC 881 has been split into multiple components according to Gomez et al. (2010).

Object	RA (h:m:s) (J2000)	Dec. (d:m:s) (J2000)	Type	S_{500} (σS_{500}) (Jy)	S_{350} (σS_{350}) (Jy)	S_{250} (σS_{250}) (Jy)	S_{160} (σS_{160}) (Jy)	S_{100} (σS_{100}) (Jy)
VCC 1	12:08:20.30	+13:41:02.0	BCD	<(0.021)	0.029 (0.005)	0.088 (0.008)	0.179 (0.033)	0.198 (0.031)
VCC 4	12:08:31.60	+15:05:42.0	Im (Im/S)	<(0.025)	<(0.024)	<(0.011)	<(0.011)	<(0.011)
VCC 9	12:09:22.30	+13:59:33.0	dE (d:E)	<(0.027)	<(0.017)	<(0.011)	<(0.015)	<(0.010)
VCC 10	12:09:24.90	+13:34:28.0	BCD	0.065 (0.019)	0.161 (0.021)	0.326 (0.032)	0.417 (0.065)	0.398 (0.058)
VCC 11	12:09:35.80	+06:44:36.0	dE (d:E)	<(0.012)*	<(0.019)	<(0.012)	–	–
VCC 12	12:09:44.30	+12:07:32.0	Sa	0.042 (0.009)	0.054 (0.008)	0.115 (0.015)	–	–
VCC 15	12:09:54.60	+13:03:00.0	Sa	0.034 (0.008)	0.061 (0.014)	0.111 (0.020)	0.020 (0.006)	0.014 (0.004)
VCC 17	12:10:01.80	+14:22:00.0	Im (Im/S)	<(0.026)*	0.041 (0.013)	0.050 (0.014)	<(0.014)	<(0.012)
VCC 20	12:10:18.90	12:19:48.00	?	<(0.020)	<(0.016)*	<(0.018)*	<(0.029)	<(0.019)
VCC 22	12:10:24.40	+13:10:14.0	BCD	<(0.022)	<(0.017)	0.024 (0.005)	0.014 (0.005)	<(0.011)
VCC 24	12:10:35.60	+11:45:39.0	BCD	<(0.024)	0.031 (0.010)	0.072 (0.009)	0.089 (0.028)	<(0.028)
VCC 25	12:10:37.50	+16:01:59.0	Sc	0.845 (0.070)	2.218 (0.165)	5.420 (0.386)	9.574 (1.153)	9.529 (1.157)
	⋮	⋮	⋮	⋮	⋮	⋮	⋮	⋮

Table C1.

Object	RA	Dec.	Type	Distance (Mpc)	T (K)	$\log(M_D/M_\odot)$	$\chi^2_{\rm d.o.f.=3}$
VCC 10	12:09:24.90	+13:34:28.0	BCD	32	19.8 (1.0)	6.4 (0.1)	3.3637
VCC 25	12:10:37.50	+16:01:59.0	Sc	32	22.5 (0.8)	7.5 (0.1)	1.3392
VCC 28	12:10:45.60	+15:51:55.0	Sc	17	17.2 (1.1)	5.7 (0.2)	2.6363
VCC 47	12:12:11.80	+13:14:48.0	Sa	32	17.6 (0.6)	7.0 (0.1)	3.4034
VCC 58	12:12:32.30	+12:07:26.0	Sb	32	17.5 (0.6)	7.4 (0.1)	2.584
VCC 73	12:13:03.00	+07:02:20.0	Sb	32	23.7 (0.8)	7.3 (0.1)	0.9731
VCC 89	12:13:47.30	+13:25:29.0	Sc	32	21.5 (0.7)	7.6 (0.1)	1.6889
VCC 92	12:13:48.30	+14:54:01.0	Sb	17	19.2 (0.5)	7.9 (0.1)	0.6288
VCC 97	12:13:53.60	+13:10:22.0	Sc	32	18.8 (0.6)	7.6 (0.1)	1.0492
VCC 99	12:14:02.10	+06:43:23.0	Sa	32	16.8 (0.7)	6.6 (0.1)	0.6295
VCC 131	12:15:04.50	+14:01:44.0	Sc	17	17.9 (0.6)	6.7 (0.1)	2.9383
VCC 135	12:15:06.70	+12:01:00.0	S/BCD	32	21.4 (1.0)	6.5 (0.1)	1.1282
VCC 143	12:15:16.10	+13:28:29.0	Sc	17	14.7 (1.6)	6.0 (0.3)	7.3118
VCC 144	12:15:18.30	+05:45:39.0	BCD	32	25.8 (1.5)	6.0 (0.1)	0.8932
VCC 157	12:15:39.30	+13:54:05.0	Sc	17	22.0 (0.6)	7.3 (0.1)	2.1474
VCC 167	12:15:54.40	+13:08:58.0	Sb	17	18.2 (0.5)	7.8 (0.1)	1.358
VCC 172	12:16:00.40	+04:39:03.0	BCD	32	17.9 (1.1)	6.2 (0.1)	2.376
VCC 199	12:16:33.70	+07:27:44.0	Sa	32	17.7 (0.5)	7.2 (0.1)	6.273
VCC 209	12:16:52.40	+14:30:55.0	dS0	17	16.8 (0.9)	5.9 (0.1)	3.5312
VCC 213	12:16:56.00	+13:37:32.0	S/BCD	17	21.7 (0.7)	6.1 (0.1)	2.2274
VCC 221	12:17:09.10	+03:40:59.0	Sc	32	22.3 (0.9)	7.1 (0.1)	1.8595
VCC 222	12:17:09.90	+07:11:30.0	Sa	32	19.3 (0.7)	6.8 (0.1)	4.0088
VCC 226	12:17:11.40	+15:19:26.0	Sc	17	21.3 (0.6)	7.1 (0.1)	2.9546
VCC 234	12:17:25.80	+06:41:24.0	Sa	32	16.2 (0.5)	7.3 (0.1)	2.9872
VCC 256	12:17:47.30	+04:28:43.0	S (dS)	32	18.1 (0.8)	6.1 (0.1)	2.975
VCC 262	12:17:55.80	+05:52:11.0	Sc	17	20.0 (0.9)	5.8 (0.1)	0.0659
VCC 267	12:17:59.90	+06:39:15.0	Sbc	23	16.1 (0.8)	7.0 (0.1)	3.2454
VCC 281	12:18:15.30	+13:44:57.0	S/BCD	17	12.9 (0.8)	6.0 (0.2)	6.3362
VCC 297	12:18:38.60	+06:42:30.0	Sc	23	17.7 (1.1)	5.9 (0.2)	2.2092
VCC 307	12:18:49.60	+14:24:59.0	Sc	17	23.0 (0.7)	8.0 (0.1)	2.2539
VCC 318	12:19:02.90	+08:51:22.0	Scd	32	17.1 (0.9)	6.8 (0.1)	1.904
VCC 323	12:19:06.50	+05:43:33.0	Sa	32	19.3 (0.6)	6.7 (0.1)	1.5232
VCC 327	12:19:12.40	+06:22:53.0	S0	32	18.8 (1.5)	6.0 (0.2)	3.9138
VCC 341	12:19:22.20	+06:05:55.0	Sa	23	17.3 (0.6)	6.8 (0.1)	2.662
VCC 362	12:19:42.30	+05:32:17.0	Sa	32	20.0 (0.5)	7.0 (0.1)	2.9277
VCC 382	12:19:56.00	+05:20:36.0	Sc	32	23.8 (0.8)	7.7 (0.1)	1.2549
VCC 393	12:20:07.50	+07:41:31.0	Sc	23	19.9 (0.7)	6.8 (0.1)	0.6081
VCC 404	12:20:17.30	+04:12:06.0	Scd	17	18.0 (0.6)	6.5 (0.1)	2.9556
VCC 406	12:20:18.70	+08:31:59.0	Sbc	17	19.1 (1.0)	5.8 (0.1)	2.3268
VCC 408	12:20:21.50	+05:23:11.0	S0	32	23.8 (1.0)	6.5 (0.1)	2.0117
VCC 411	12:20:24.30	+05:34:22.0	S0	23	19.2 (1.0)	6.0 (0.1)	3.5458
VCC 415	12:20:25.20	+06:54:32.0	Sd	23	16.8 (0.9)	6.3 (0.2)	4.7429
VCC 419	12:20:29.50	+10:14:42.0	Sb	17	20.8 (1.5)	5.8 (0.1)	3.564
VCC 434	12:20:48.50	+05:38:23.0	S (dS)	23	19.9 (0.6)	6.4 (0.1)	0.0482
VCC 449	12:21:02.30	+03:43:19.0	Sbc	17	18.2 (0.6)	6.9 (0.1)	7.636
VCC 450	12:21:03.70	+07:04:40.0	S0	23	19.5 (1.0)	6.0 (0.1)	2.7179
VCC 462	12:21:16.40	+04:35:44.0	S0a - S0/Sa	17	21.1 (0.8)	6.0 (0.1)	1.3394
VCC 479	12:21:29.00	+08:09:03.0	?	23	13.1 (0.7)	6.3 (0.2)	2.0121
VCC 483	12:21:32.80	+14:36:22.0	Sc	17	20.7 (0.6)	7.4 (0.1)	2.9491
VCC 491	12:21:40.90	+11:30:12.0	Scd	17	21.2 (0.9)	6.7 (0.1)	6.2223
VCC 492	12:21:41.50	+05:23:05.0	Sa	23	20.6 (0.7)	6.4 (0.1)	2.64
VCC 497	12:21:42.50	+14:35:52.0	Sc	17	19.2 (0.5)	7.7 (0.1)	3.1475
VCC 508	12:21:54.90	+04:28:25.0	Sc	17	22.8 (0.7)	7.9 (0.1)	0.289
VCC 517	12:22:01.30	+05:06:00.0	Sab	17	20.5 (0.8)	6.1 (0.1)	3.5618
VCC 524	12:22:05.60	+09:02:37.0	Sbc	23	19.8 (0.5)	7.3 (0.1)	2.8402
VCC 534	12:22:12.40	+07:08:39.0	Sa	23	19.3 (0.8)	6.8 (0.1)	5.9347
VCC 552	12:22:27.20	+04:33:59.0	Sc	17	18.4 (1.1)	6.5 (0.1)	6.8967

Table C1 *– continued*

Object	RA	Dec.	Type	Distance (Mpc)	T (K)	$\log(M_D/M_\odot)$	$\chi^2_{\text{d.o.f.}=3}$
VCC 559	12:22:31.30	+15:32:17.0	Sab	17	22.4 (0.7)	6.8 (0.1)	5.3575
VCC 568	12:22:39.70	+06:13:34.0	S (dS)	23	16.2 (1.0)	6.1 (0.1)	3.5565
VCC 570	12:22:38.50	+11:48:03.0	Sab	17	20.3 (0.5)	6.9 (0.1)	3.5497
VCC 571	12:22:41.10	+07:57:01.0	S0	23	16.2 (1.0)	5.9 (0.2)	1.0217
VCC 576	12:22:42.20	+09:19:57.0	Sbc	23	20.1 (0.6)	7.3 (0.1)	0.6984
VCC 596	12:22:54.90	+15:49:21.0	Sc	17	21.5 (0.6)	8.1 (0.1)	2.0706
VCC 613	12:23:06.20	+05:15:02.0	Sa	17	19.0 (0.5)	6.7 (0.1)	1.77
VCC 630	12:23:17.20	+11:22:05.0	Sd	17	18.2 (0.5)	7.0 (0.1)	1.7
VCC 656	12:23:38.70	+06:57:15.0	Sb	23	19.8 (0.6)	7.2 (0.1)	1.1153
VCC 664	12:23:44.50	+12:28:42.0	Sc	17	18.1 (0.6)	6.4 (0.1)	3.8602
VCC 667	12:23:48.50	+07:11:13.0	Sc	23	17.4 (0.5)	6.8 (0.1)	0.2692
VCC 672	12:23:53.50	+07:06:26.0	S0	23	17.3 (0.5)	5.9 (0.1)	1.5383
VCC 688	12:24:00.10	+07:47:06.0	Sc	23	18.9 (0.6)	6.5 (0.1)	2.5243
VCC 690	12:24:02.20	+05:18:45.0	S (dS)	17	20.8 (1.0)	5.8 (0.1)	4.2232
VCC 692	12:24:01.50	+12:12:17.0	Sc	17	19.5 (0.6)	6.6 (0.1)	0.2166
VCC 693	12:24:03.20	+05:10:51.0	Sm	17	17.2 (0.7)	5.8 (0.1)	1.6154
VCC 697	12:24:05.50	+07:02:29.0	Sc	23	18.6 (0.6)	6.6 (0.1)	1.3084
VCC 699	12:24:07.40	+06:36:27.0	Pec	23	21.0 (1.0)	6.5 (0.1)	6.2302
VCC 713	12:24:14.50	+08:32:09.0	Sc	23	20.1 (0.7)	6.7 (0.1)	1.6325
VCC 734	12:24:33.60	+06:42:44.0	Sbc	17	18.3 (1.1)	5.8 (0.2)	5.8596
VCC 737	12:24:39.40	+03:59:44.0	S/BCD	17	16.6 (1.0)	5.9 (0.2)	2.1592
VCC 739	12:24:40.00	+03:18:10.0	Sd	17	18.1 (1.1)	6.1 (0.1)	6.5397
VCC 741	12:24:41.30	+03:43:17.0	BCD	17	19.7 (2.4)	5.2 (0.3)	4.5118
VCC 758	12:24:54.90	+07:26:40.0	S0	23	22.2 (0.7)	6.8 (0.1)	2.7338
VCC 781	12:25:15.20	+12:42:53.0	dS0	17	19.0 (1.6)	5.4 (0.2)	1.1692
VCC 785	12:25:18.10	+04:55:30.0	Sa	17	16.6 (0.4)	7.1 (0.1)	4.8788
VCC 787	12:25:18.00	+05:44:28.0	Scd	23	19.9 (0.8)	6.7 (0.1)	3.6289
VCC 792	12:25:22.20	+10:01:01.0	Sab	23	18.2 (0.4)	7.4 (0.1)	5.2217
VCC 809	12:25:33.10	+12:15:37.0	Sc	17	15.5 (0.6)	6.5 (0.1)	3.0928
VCC 827	12:25:42.60	+07:13:00.0	Sc	23	18.8 (0.6)	7.4 (0.1)	5.7799
VCC 834	12:25:46.70	+04:30:35.0	Sc	17	18.3 (0.8)	6.3 (0.1)	5.6106
VCC 836	12:25:46.70	+12:39:44.0	Sab	17	23.5 (0.9)	7.1 (0.1)	2.5965
VCC 841	12:25:47.40	+14:57:09.0	BCD	17	20.5 (1.4)	5.4 (0.1)	0.5943
VCC 849	12:25:50.70	+10:27:33.0	Sbc	23	19.1 (0.7)	7.0 (0.1)	5.468
VCC 851	12:25:54.10	+07:33:17.0	Sc	23	18.9 (0.6)	7.0 (0.1)	2.579
VCC 859	12:25:58.30	+03:25:49.0	Sc	17	17.4 (0.6)	7.0 (0.1)	6.1862
VCC 873	12:26:07.50	+13:06:46.0	Sc	17	21.0 (0.6)	7.4 (0.1)	2.1181
VCC 888	12:26:18.50	+08:20:59.0	Im (Im/S)	23	13.8 (2.8)	6.2 (0.5)	6.5656
VCC 905	12:26:30.10	+08:52:20.0	Sc	23	17.5 (0.7)	6.9 (0.1)	3.1603
VCC 912	12:26:32.20	+12:36:40.0	Sbc	17	19.7 (0.6)	6.8 (0.1)	0.5869
VCC 921	12:26:36.10	+03:57:53.0	Sbc	17	23.9 (0.8)	6.6 (0.1)	1.5483
VCC 938	12:26:46.70	+07:55:08.0	Sc	17	20.4 (0.6)	6.7 (0.1)	1.4266
VCC 979	12:27:11.60	+09:25:14.0	Sa	23	24.5 (0.9)	6.8 (0.1)	1.7719
VCC 995	12:27:22.20	+10:52:00.0	Sc	17	14.9 (1.2)	6.0 (0.2)	2.0003
VCC 1002	12:27:26.40	+06:15:46.0	Sc	23	19.6 (0.6)	7.2 (0.1)	0.9396
VCC 1030	12:27:40.50	+13:04:44.0	S0	17	23.9 (0.9)	6.4 (0.1)	0.9699
VCC 1043	12:27:45.60	+13:00:32.0	Sb	17	20.5 (0.6)	7.2 (0.1)	0.9814
VCC 1048	12:27:55.40	+05:43:16.0	Scd	23	19.4 (0.8)	6.5 (0.1)	2.495
VCC 1086	12:28:15.90	+09:26:11.0	S (dS)	23	19.0 (0.5)	6.8 (0.1)	4.3639
VCC 1091	12:28:18.80	+08:43:46.0	Sbc	23	19.3 (0.7)	6.5 (0.1)	4.2775
VCC 1118	12:28:40.50	+09:15:32.0	Sc	23	23.0 (0.8)	6.8 (0.1)	1.0827
VCC 1154	12:29:00.00	+13:58:43.0	S0	17	25.9 (0.9)	6.3 (0.1)	3.1325
VCC 1189	12:29:28.80	+06:46:18.0	Sc	17	17.0 (0.6)	6.5 (0.1)	1.0915
VCC 1190	12:29:28.00	+08:45:00.0	Sa	23	21.9 (0.7)	6.8 (0.1)	1.9899
VCC 1193	12:29:30.60	+07:41:48.0	Sc	17	18.6 (0.8)	6.4 (0.1)	6.9848
VCC 1200	12:29:35.20	+10:47:35.0	Im (Im/S)	17	13.5 (0.8)	5.8 (0.2)	0.9605
VCC 1205	12:29:37.80	+07:49:27.0	Sc	17	22.2 (0.8)	6.6 (0.1)	0.7719
VCC 1250	12:29:59.10	+12:20:55.0	S0	17	23.5 (0.9)	6.0 (0.1)	0.9502
VCC 1253	12:30:02.20	+13:38:11.0	S0a - S0/Sa	17	25.5 (1.2)	5.7 (0.1)	1.8314
VCC 1290	12:30:26.80	+04:14:48.0	Sb	17	19.7 (0.6)	6.9 (0.1)	1.7848

Table C1 – *continued*

Object	RA	Dec.	Type	Distance (Mpc)	T (K)	$\log(M_D/M_\odot)$	$\chi^2_{\rm d.o.f.=3}$
VCC 1326	12:30:57.10	+11:29:01.0	Sa	17	26.4 (1.4)	6.0 (0.1)	1.0426
VCC 1330	12:30:59.70	+08:04:41.0	Sa	17	18.4 (0.6)	6.6 (0.1)	1.1004
VCC 1356	12:31:22.90	+11:29:33.0	Sm/BCD	17	18.1 (1.7)	5.6 (0.2)	1.8336
VCC 1374	12:31:38.00	+14:51:24.0	Im/BCD	17	18.1 (1.0)	5.9 (0.1)	3.009
VCC 1401	12:31:59.20	+14:25:14.0	Sbc	17	21.3 (0.6)	8.0 (0.1)	2.1846
VCC 1419	12:32:10.50	+13:25:11.0	S (dS)	17	18.5 (0.8)	6.1 (0.1)	0.7018
VCC 1437	12:32:33.50	+09:10:25.0	BCD	17	25.3 (1.4)	5.4 (0.1)	1.4448
VCC 1450	12:32:41.70	+14:03:06.0	Sc	17	19.4 (0.7)	6.8 (0.1)	4.0079
VCC 1486	12:33:10.00	+11:20:51.0	S (dS)	17	19.5 (1.0)	5.8 (0.1)	2.7726
VCC 1508	12:33:30.30	+08:39:16.0	Sc	17	20.2 (0.8)	7.1 (0.1)	4.2483
VCC 1516	12:33:39.70	+09:10:30.0	Sbc	17	19.7 (0.7)	6.9 (0.1)	3.9513
VCC 1535	12:34:03.00	+07:41:57.0	S0	17	23.8 (0.8)	7.0 (0.1)	1.6852
VCC 1552	12:34:15.80	+13:04:32.0	Sa	17	19.3 (0.6)	6.6 (0.1)	5.1485
VCC 1555	12:34:20.30	+08:11:52.0	Sc	17	19.8 (0.6)	7.9 (0.1)	0.679
VCC 1566	12:34:30.70	+09:09:17.0	Sd	17	14.9 (1.0)	6.2 (0.2)	3.506
VCC 1575	12:34:39.50	+07:09:37.0	Sm	17	20.8 (0.7)	6.5 (0.1)	0.5833
VCC 1673	12:36:32.70	+11:15:29.0	Sc	17	21.5 (0.9)	7.3 (0.1)	3.9681
VCC 1676	12:36:34.20	+11:14:20.0	Sc	17	23.1 (0.9)	7.6 (0.1)	5.0486
VCC 1686	12:36:43.50	+13:15:34.0	Sm	17	17.2 (0.6)	6.7 (0.1)	4.2347
VCC 1690	12:36:49.80	+13:09:46.0	Sab	17	21.2 (0.6)	7.6 (0.1)	4.488
VCC 1727	12:37:43.50	+11:49:05.0	Sab	17	20.5 (0.6)	7.6 (0.1)	2.2168
VCC 1758	12:38:21.00	+07:53:31.0	Sc	17	16.3 (0.7)	6.4 (0.1)	2.6176
VCC 1791	12:39:25.00	+07:57:57.0	Sm/BCD	17	17.4 (1.0)	6.1 (0.1)	1.8751

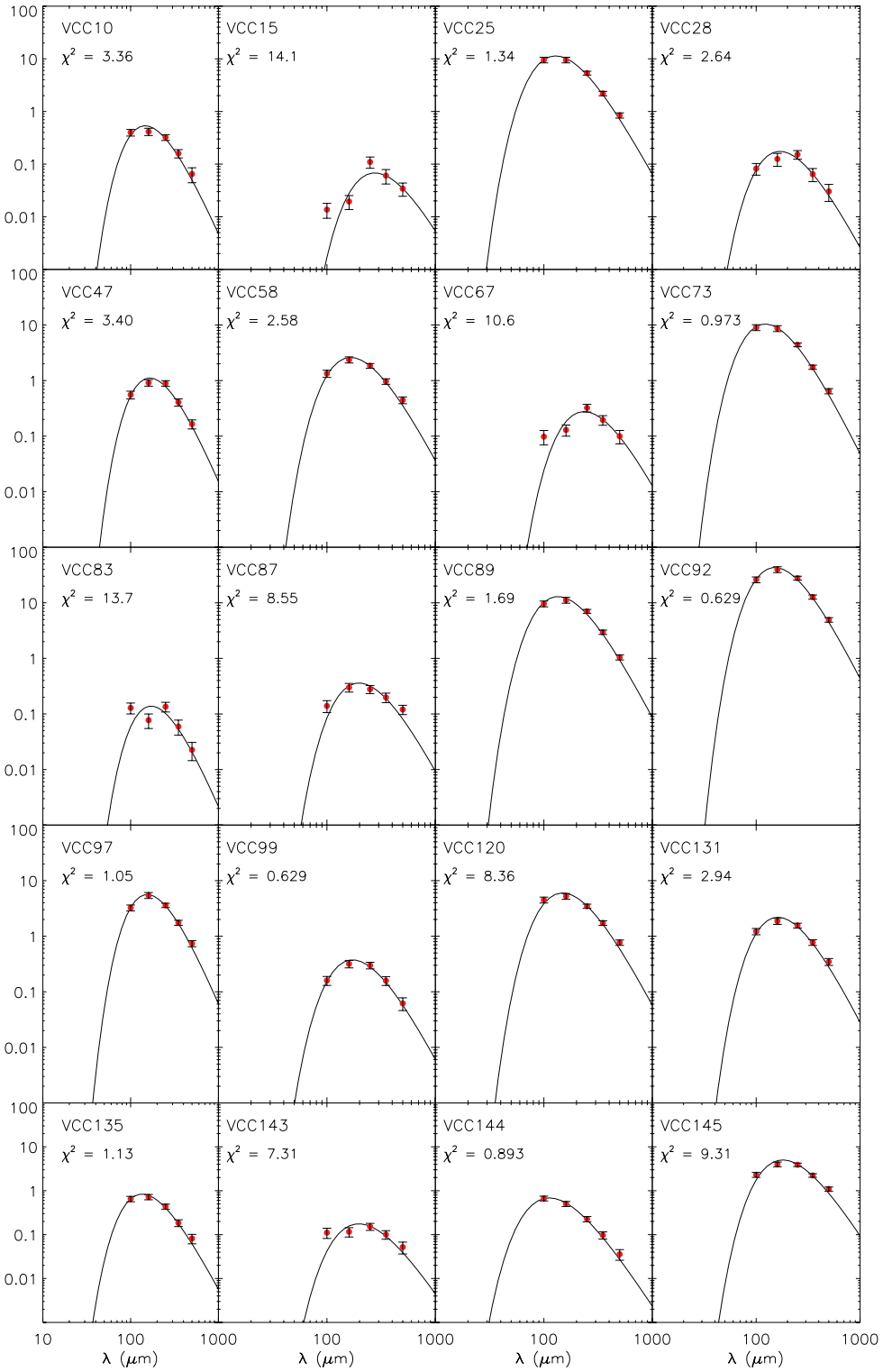

Figure D1. FIR SED plots for the VCC galaxies with five-band FIR detections. Also shown are the single-temperature modified blackbody fits (solid black line).

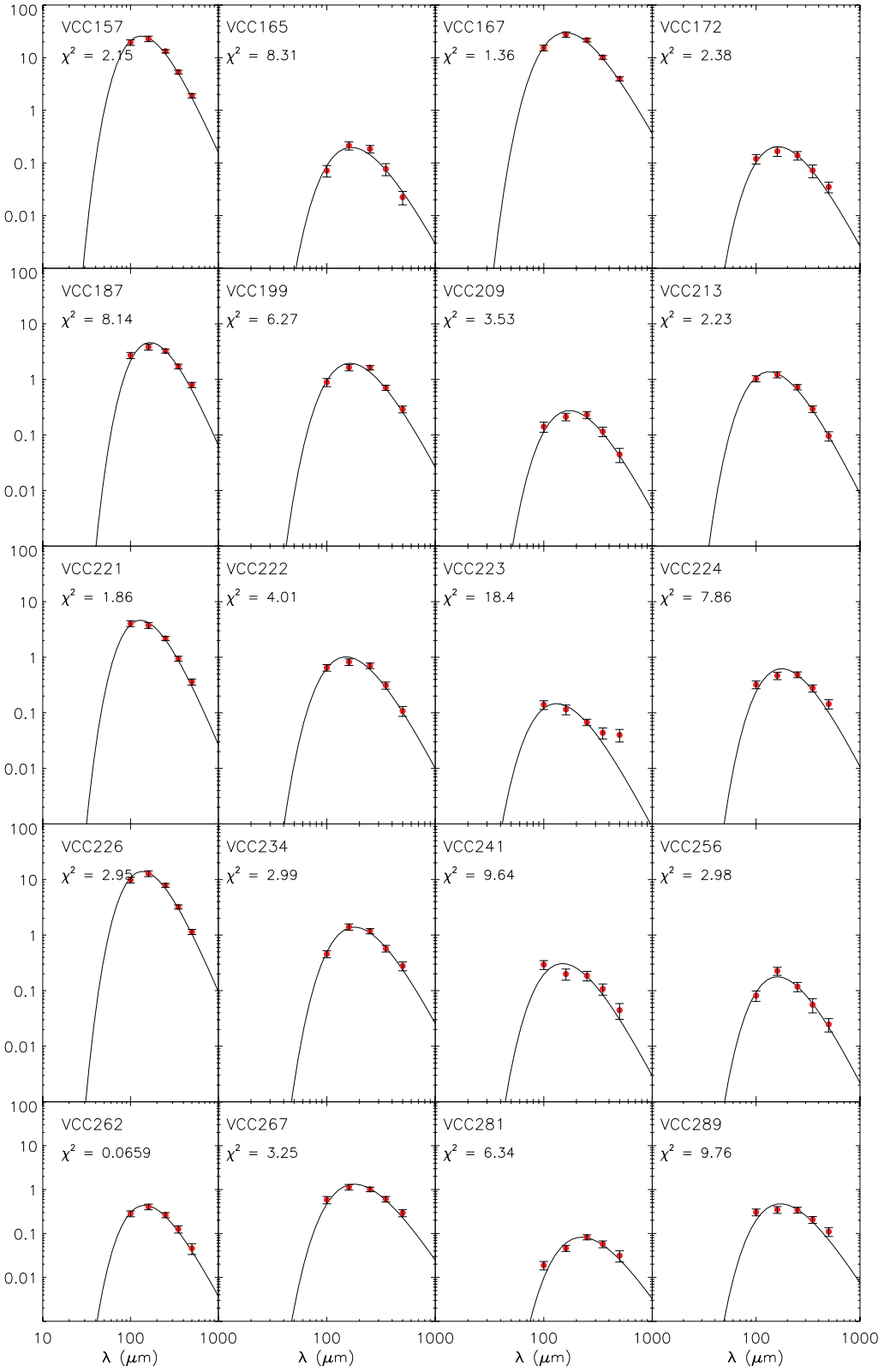

Figure D1 – *continued*

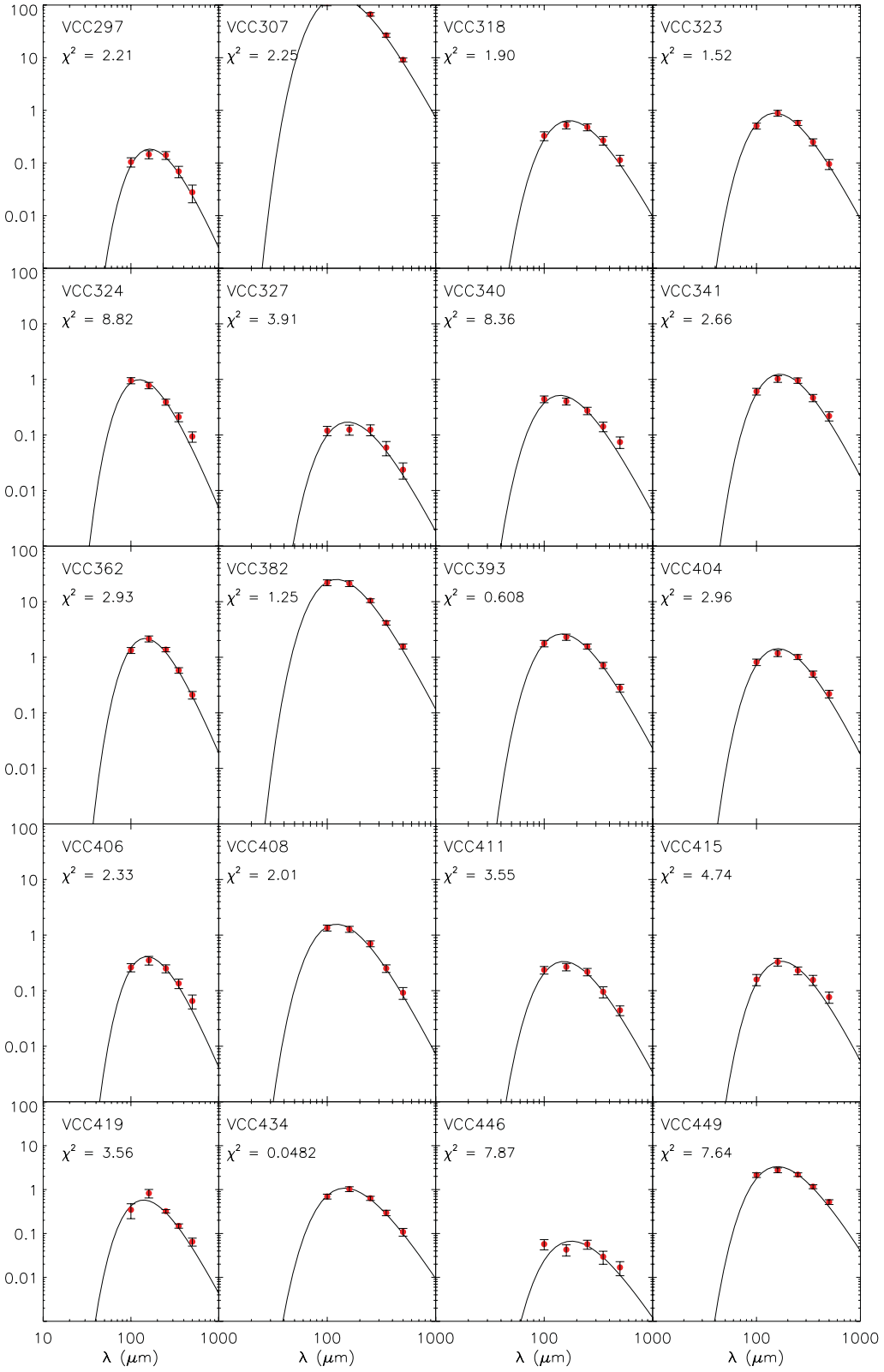

Figure D1 – *continued*

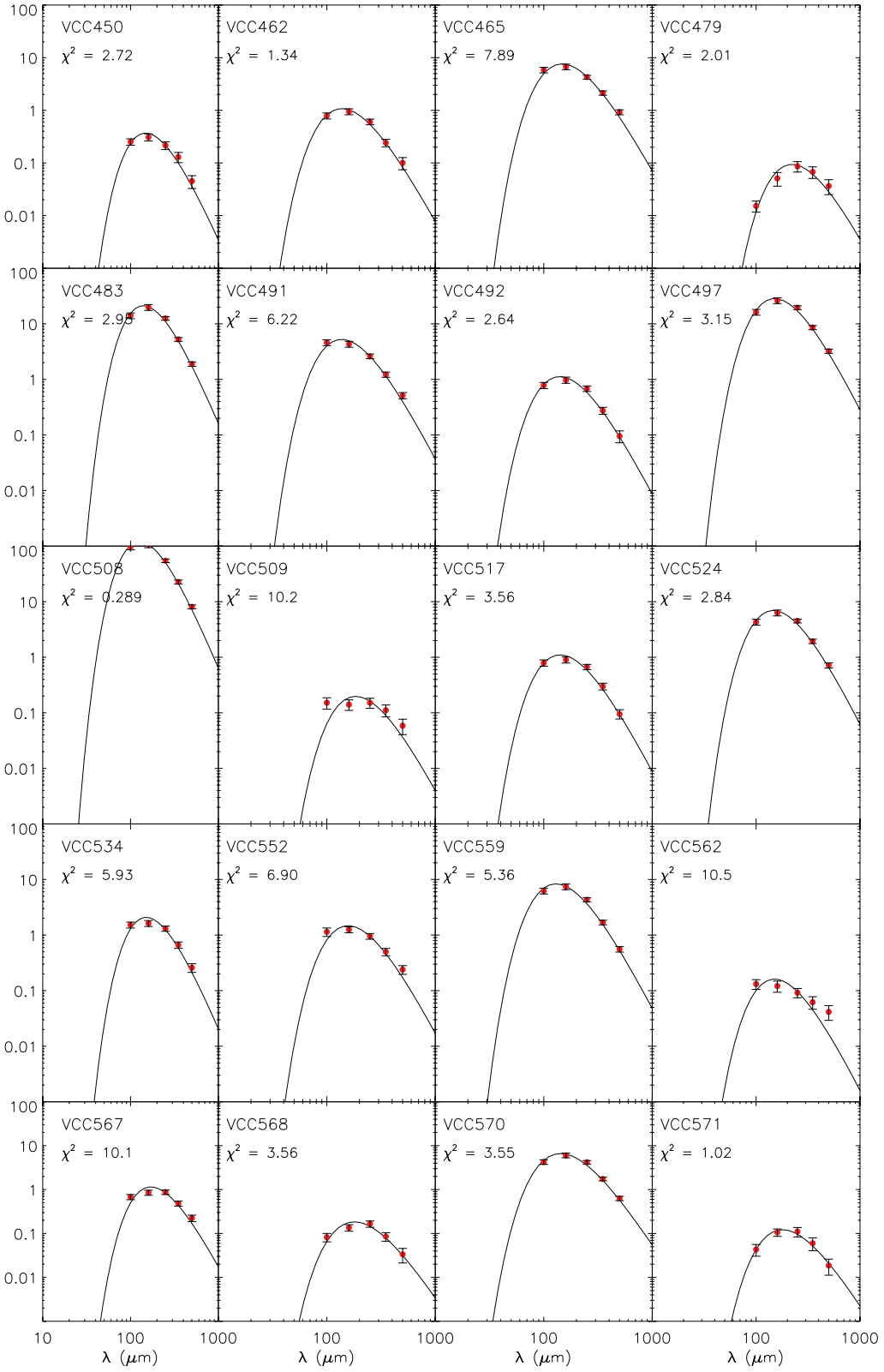

Figure D1 – *continued*

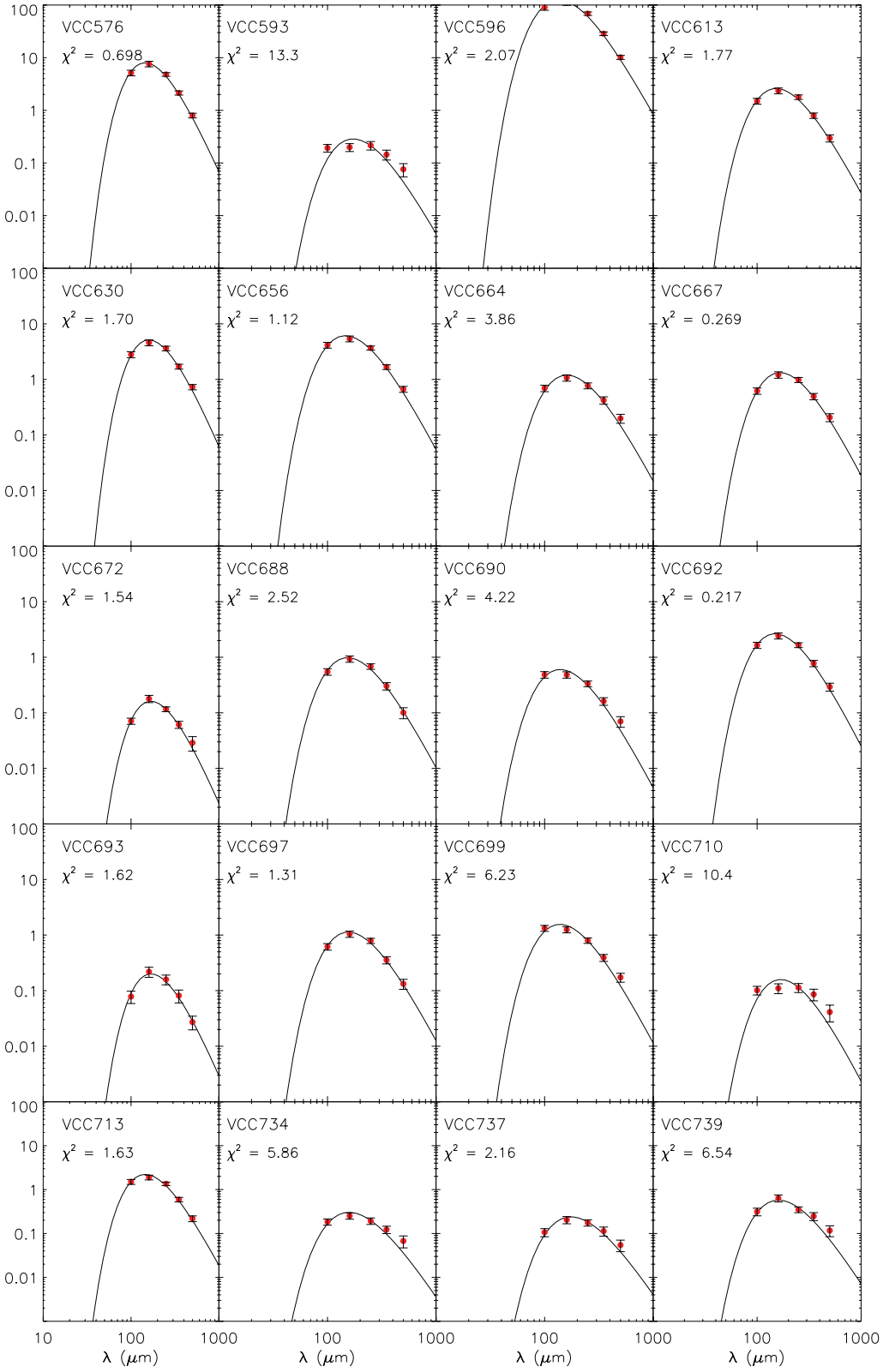

Figure D1 – *continued*

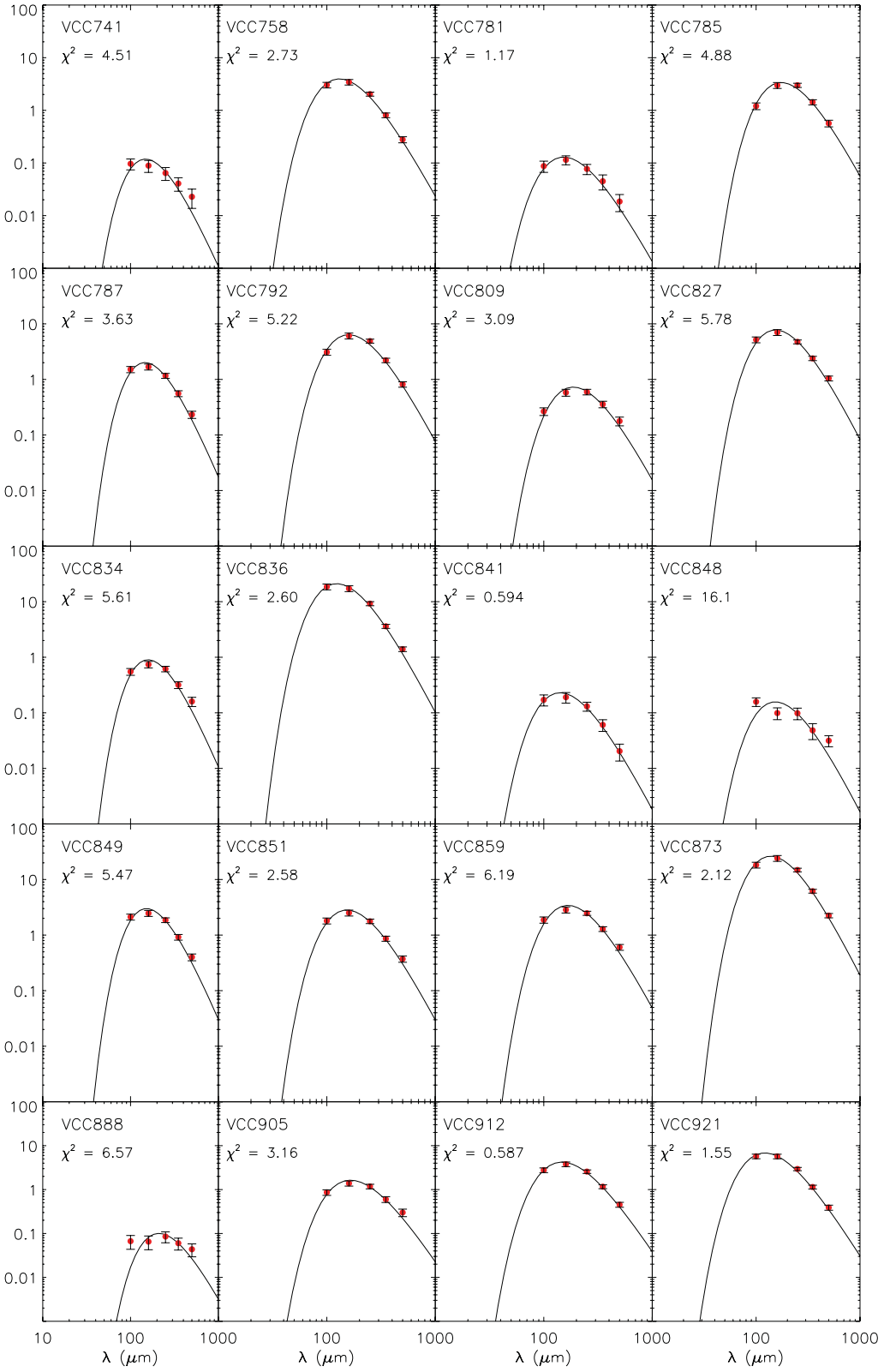

Figure D1 – *continued*

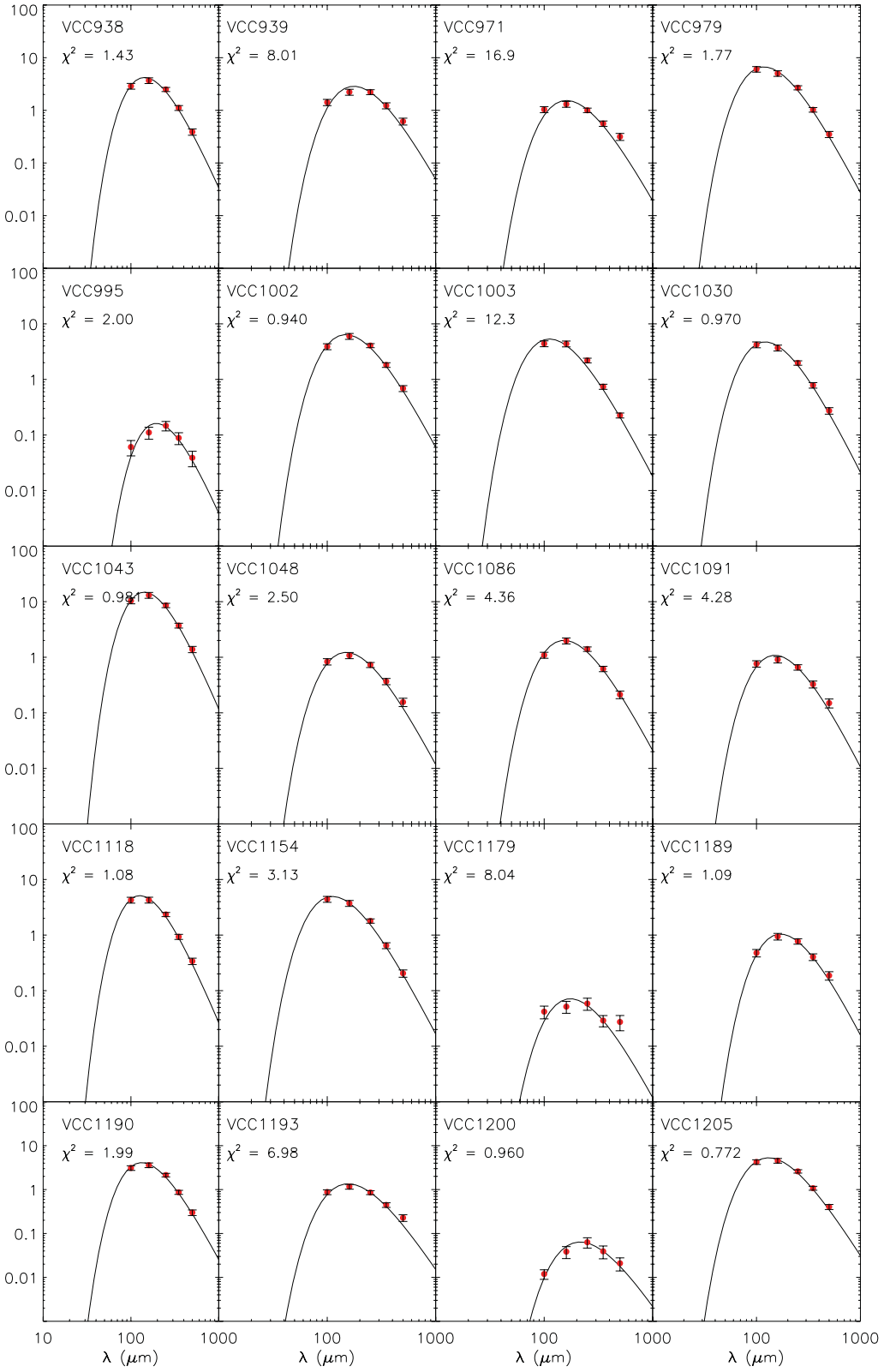

Figure D1 – *continued*

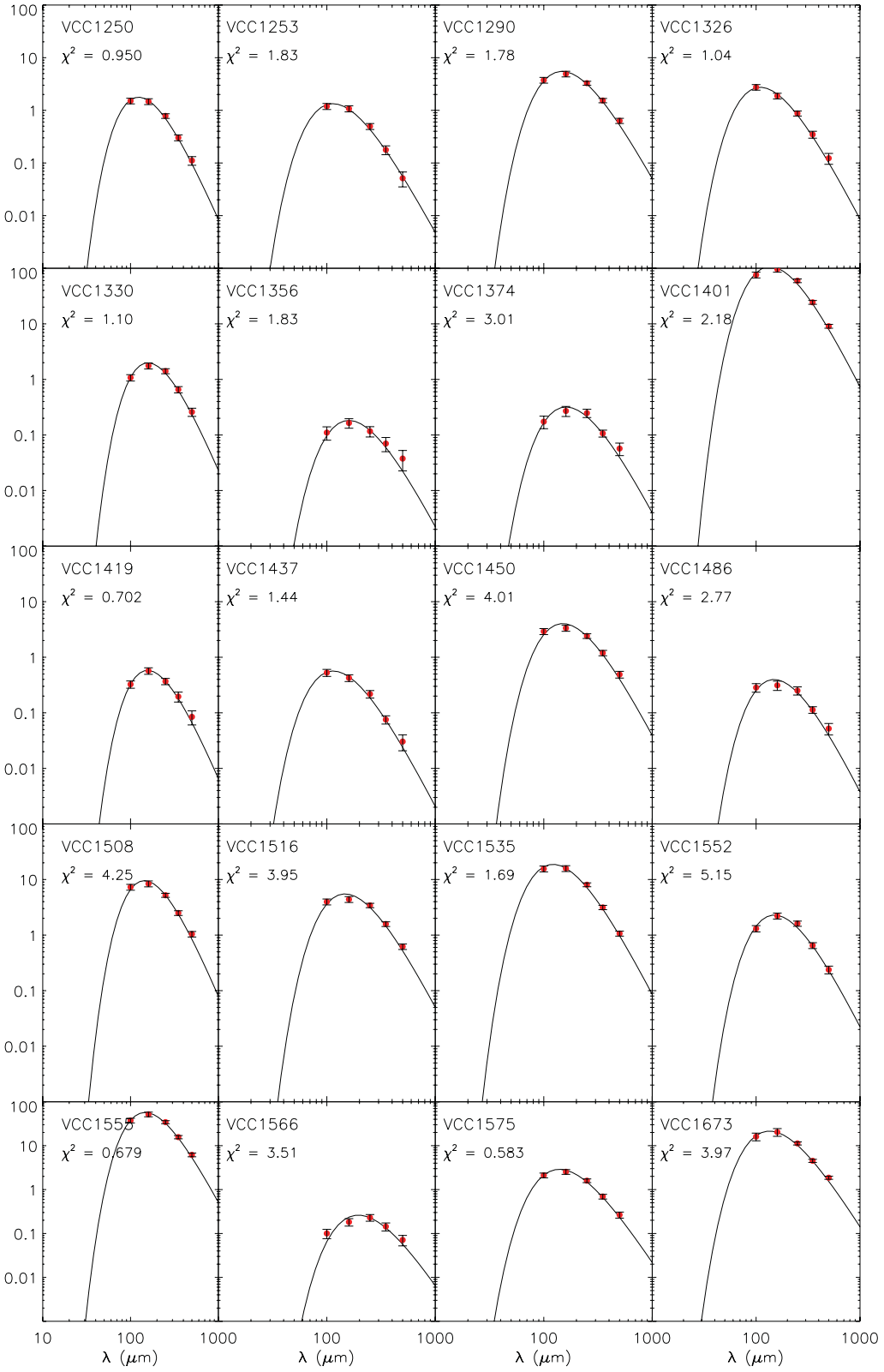

Figure D1 – *continued*

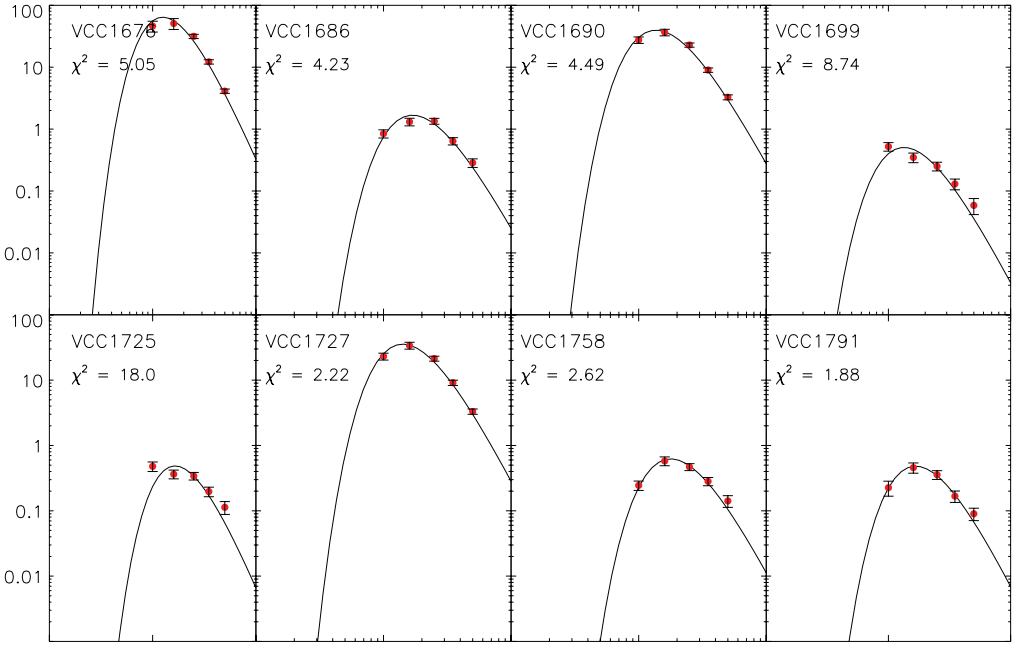

Figure D1 – *continued*

SUPPORTING INFORMATION

Additional Supporting Information may be found in the online version of this article:

Table B1. Five-band FIR detections and upper limits for the VCC galaxies (http://mnras.oxfordjournals.org/lookup/suppl/doi:10.1093/mnras/sts125/-/DC1).

Please note: Oxford University Press are not responsible for the content or functionality of any supporting materials supplied by the authors. Any queries (other than missing material) should be directed to the corresponding author for the article.

This paper has been typeset from a TEX/LATEX file prepared by the author.